Characterization of air-void systems in 3D printed cementitious materials using optical image scanning and X-ray computed tomography

Chen, Yu; Çopuroğlu, Oğuzhan; Romero Rodriguez, Claudia; França de Mendonça Filho, F.; Schlangen, Erik

DOI
10.1016/j.matchar.2021.110948

Publication date
2021

Document Version
Final published version

Published in
Materials Characterization

Citation (APA)
Chen, Y., Çopuroğlu, O., Romero Rodriguez, C., França de Mendonça Filho, F., & Schlangen, E. (2021). Characterization of air-void systems in 3D printed cementitious materials using optical image scanning and X-ray computed tomography. *Materials Characterization*, *173*, 1-18. Article 110948. https://doi.org/10.1016/j.matchar.2021.110948

Materials Characterization 173 (2021) 110948

Contents lists available at ScienceDirect

Materials Characterization

journal homepage: www.elsevier.com/locate/matchar

Characterization of air-void systems in 3D printed cementitious materials using optical image scanning and X-ray computed tomography

Yu Chen *, Oğuzhan Çopuroğlu, Claudia Romero Rodriguez, Fernando F. de Mendonca Filho, Erik Schlangen

Microlab, Faculty of Civil Engineering and Geosciences, Delft University of Technology, Stevinweg 1, 2628CN Delft, the Netherlands

ARTICLE INFO

Keywords:
Air void
3D printed cementitious materials
Optical image scanning
X-ray computed tomography
Image analysis
Interlayer

ABSTRACT

For many 3D printed cementitious materials, air voids may play a dominant role in the interlayer bond strength. However, to date, far too little attention has been paid to reveal the air void characteristics in 3D printed cementitious materials. Therefore, to fill this gap, this study attempts to provide an example of systematically characterizing the typical air void system of 3D printed cementitious materials via different image acquisition and analysis techniques. Two printable limestone and calcined clay-based mixtures were employed to prepare the printed samples. The micrographs were acquired by using optical image scanning and X-ray computed tomography. Afterwards, air void metrics in printed cementitious materials were determined, i.e., content, distribution, size, and shape. The results revealed that most of the air voids with the diameter in the range of 10–1000 μm were distributed evenly in the layer region of printed samples. Large air voids (1000–6000 μm) were enclosed mainly between the printed filaments (interface region), which resulted in the relatively higher local porosity than that of layer region. Additionally, the majority of air voids displayed irregular and elongated shapes, which could be attributed to the extrusion and layer-wise manufacturing processes in 3D printing. Finally, a comparison between optical image scanning and X-ray computed tomography was given.

1. Introduction

Over the last years, there has been an exponentially increasing interest in the research of extrusion-based 3D concrete printing (3DCP) [1–5]. The working mechanism of 3DCP can be explained as linear filaments being deposited layer by layer to fabricate customized components without the aid of formwork [6–8]. The use of 3DCP in concrete construction brings many advantages, for example, minimal labor, fast fabrication, fewer construction wastes, cost-effectiveness, formwork-free construction, and increased flexibility of architectural design [1,2,8,9]. In comparison with mold-cast concrete, elimination of formwork is one of the most significant benefits from 3DCP, which also induces many challenges on fresh-state behaviors of printable cementitious materials [4,10]. In this context, the fresh mixtures must meet the contradicting rheological demands, for instance, proper fluidity during extrusion, and adequate stability and viscosity during the layer-by-layer deposition process [9,11]. Owing to the differences in fresh properties and manufacturing processes, the air void system in 3D printed cementitious materials should differ from that of the mold-cast cementitious materials. According to Aïtcin [12], the viscosity of paste, the size of coarse aggregate, the consistency of fresh mixture, and the condition of vibration and compaction influence the formation of entrapped air voids in hardened concrete. As reported by [13,14], the viscosity of fresh mixtures for 3DCP may be higher than that of mold-cast concrete to avoid water drainage and ensure the stability of the layered structure during the printing process. Also, there are no vibration and compaction processes in 3DCP. The extrusion process in 3DCP may influence the air void parameters, such as shape, size, and distribution.

For implementing 3DCP in building construction, the investigation into the mechanical performance of 3D printed cementitious materials needs to be prioritized. The strength and elasticity of hardened cementitious materials are mainly influenced by capillary pores and air voids [15,16]. For mold-cast concrete, increasing about 1% of air voids could lead up to a 4–5% reduction in the compressive strength [17,18]. Due to the layer-wise manufacturing processes, many interlayers were formed

* Corresponding author.
E-mail addresses: Y.Chen-6@tudelft.nl (Y. Chen), O.Copuroglu@tudelft.nl (O. Çopuroğlu), C.RomeroRodriguez@tudelft.nl (C. Romero Rodriguez), F.Filho@tudelft.nl (F.F. Mendonca Filho), Erik.Schlangen@tudelft.nl (E. Schlangen).

https://doi.org/10.1016/j.matchar.2021.110948
Received 19 May 2020; Received in revised form 16 December 2020; Accepted 3 February 2021
Available online 6 February 2021

in a 3D printed structure. The interlayer bonding (also known as interface adhesion) is considered as a weakness of the 3D printed structure [6,19,20], which is attributed to the limited intermixing between two subsequent layers [21]. High amount of air voids between the layers as a typical phenomenon can be found in many 3D printed cementitious materials with a weak interface adhesion [20,22,23]. Under scanning electron microscope, Nerella et al. [20] observed many longitudinal cavities induced by entrapped air voids between two layers in their printed sample that showed weak mechanical performance. Similarly, others [22,24] reported that increasing the air void content in the interlayer region could result in a severe reduction of interface adhesion. Therefore, for some 3D printed cementitious materials, air voids may play a dominant role in the interlayer bond strength. Quantitative air void characterization of 3D printed cementitious materials becomes quite essential for assessing and predicting the corresponding mechanical performance. Additionally, the air void analysis could be considered as a useful method for selecting the optimal mix design and printing parameters (e.g., time intervals between layers, nozzle standoff distances, printing speeds, and others) for 3DCP research.

The air void characterization of mold-cast concrete is typically done using both fresh and hardened cementitious materials. Ley et al. [25] proposed an approach to measure the size and spacing factor of air voids in fresh concrete. However, analysis of air voids in hardened cementitious materials appears more frequently in literature. As indicated in earlier studies [26–28], digital image acquisition and processing is a powerful tool, widely implemented to investigate the microstructure of materials. The air voids in hardened cementitious materials can be rapidly determined via stereological examination of polished sections or thin sections using an optical microscope or flatbed scanner, and quantified by 2D/1D approaches (e.g., linear-traverse method, and point-count method from ASTM C457–98 [29]), as reported by [16,18,26,30–33]. However, air bubbles are distributed in a 3D space of hardened cementitious materials. Only using the 2D approach could not indicate anisotropy/heterogeneity of air voids in studied samples. X-ray computed tomography was therefore employed by many researchers [34–38] for acquiring digital images that allowed assessing the 3D heterogeneity of air void structure. A critical review about applying X-ray computed tomography to characterize the porosity/void of concrete and asphalt is given by du Plessis and Boshoff [39]. The authors highlighted the contradiction between the obtained image resolution (capability of the minimum pore size) and the dimension of sample (characterization of macropores).

In the case of 3D printed cementitious materials, earlier studies [40,41] have attempted to determine the air void content using X-ray computed tomography scanning and image analysis. However, to our knowledge, few researchers have been able to draw on any systematic research into characterizing air void system of 3D printed cementitious materials. On the other hand, optical microscope (or scanner) is widely available in the majority of laboratories, whereas micro-computed tomography (Micro-CT) scanner is not. Thus, it is worthwhile to explore to what extent can the air void characteristics of 3D printed cementitious materials be reliably determined using optical microscopy (or scanning) for thin- and polished-section analyses, in comparison with X-ray computed tomography.

The objective of this paper is to systematically characterize the typical air void system of 3D printed cementitious materials via digital image analysis. Two limestone and calcined clay-based 3D printable cementitious materials with different interlayer properties that were developed in our earlier study [42] were used to prepare the printed samples. Optical image scanning and X-ray computed tomography, as two distinct techniques, were employed to acquire digital images. Afterwards, binary images, containing only air voids, were segmented from the obtained images. Air voids of 3D printed cementitious materials could therefore be studied in characteristics of content, distribution, size, and shape by different approaches. Additionally, a discussion about possible reasons for air void formation in printed cementitious materials is offered. Furthermore, a comparison between the two employed methodologies, optical image scanning and X-ray computed tomography, is given.

Table 1
Mixture proportions of printable cementitious materials (by weight of binder).

	Binder				Water	Sand	SP	VMA
	PC	LP	Calcined clay					
			HGCC	LGCC				
M1	0.4	0.2	0.2	0.2	0.3	1.5	0.02	0.0024
M2	0.4	0.2	0.1	0.3	0.3	1.5	0.02	0.0024

2. Materials and methods

2.1. Printable mixture design

Two printable mixtures that were developed by the authors [42] were used in the current study. As shown in Table 1, the binder of each mixture was a blend of three primary materials, i.e., 40 wt% of CEM I 52.5R Portland cement (PC), 20 wt% of limestone powder (LP), and 40 wt% of calcined clay. Up to 2 mm of grain size of quartz sand was selected as the aggregate. Except for the type of calcined clay, both mixture compositions were kept identical, for instance, sand to binder ratio of 1.5, water to binder ratio of 0.3, 2 wt% (of the binder mass) of polycarboxylate ether-based superplasticizer (SP), and 0.24 wt% (of the binder mass) of viscosity-modifying admixture (VMA). Two types of calcined clays: a low-grade (LGCC: 48.8 wt% of the reactive part), and a high-grade (HGCC: 75.1 wt% of the reactive part) were employed. The average particle diameter (D_{v50}) of PC, LP, LGCC, and HGCC was 14.86 μm, 24.19 μm, 69.35 μm, and 3.75 μm, respectively. The calcined clay in mixture M1 was a blend of LGCC and HGCC with a mass ratio of 1:1. For mixture M2, the mass ratio (LGCC/HGCC) was 3:1. The oxide composition of all binding materials determined by X-ray fluorescence (XRF) was presented in Table 2.

2.2. Sample preparation

For the printing operation, a lab-scale 3DCP setup that was introduced by previous studies [9,42] was used (see Fig. 1 (a)). A hybrid down- and back-flow based nozzle with a rectangle opening (width: 40 mm; height: 12 mm) was adopted in this study to print the filament with the rectangular cross-section. The fresh mixture was prepared by following protocols in Table 3. Based on fixed printing parameters (Table 4), a beam that contained 5 vertically stacked layers was manufactured per mixture. The length of each layer was 900 mm. For the first 24 h after printing, the printed beam was cured under the plastic film at the ambient environment (20 ± 2 °C, and about 55% relative humidity). After that, the sample was stored in a fog room with 20 ± 2 °C, and 99% relative humidity until it was 28-day-old. The samples for air void analysis were extracted at the end of the curing.

The dimensions and extracted positions of the specimens are illustrated in Fig. 1 (b). Note that, each specimen contained three interlayer regions. The specimen preparation of thin sections was derived from earlier studies [43,44]. Before polishing, the extracted prisms were impregnated by using low-viscosity epoxy with fluorescent pigment. Standard thin sections with a thickness of 30 μm (approximately 27 μm of cementitious material, and 3 μm of mounting glue) were obtained via a semi-automatic thin sectioning machine. Lab-grade ethanol was utilized as coolant during processes of cutting, grinding, and polishing. For X-ray computed tomography (CT) scanning, cylindrical samples (Ø 25 mm; height: 40 mm) were drilled and sawn from the printed beam.

Table 2
The chemical composition of PC, LP, LGCC, and HGCC determined by XRF. Based on internal standards.

Material	CaO [wt%]	SiO_2 [wt%]	Al_2O_3 [wt%]	Fe_2O_3 [wt%]	K_2O [wt%]	TiO_2 [wt%]	ZrO_2 [wt%]	Other [wt%]	Total [wt%]
PC	68.7	17.4	4.1	2.8	0.6	0.3	0	6.1	100
LP	39.6	0.2	0	0.1	0	0	0	60.1	100
LGCC	0.6	55.1	38.4	2.6	0.2	1.1	0.1	1.9	100
HGCC	0	47.3	50.6	0.5	0.2	1.3	0	0.1	100

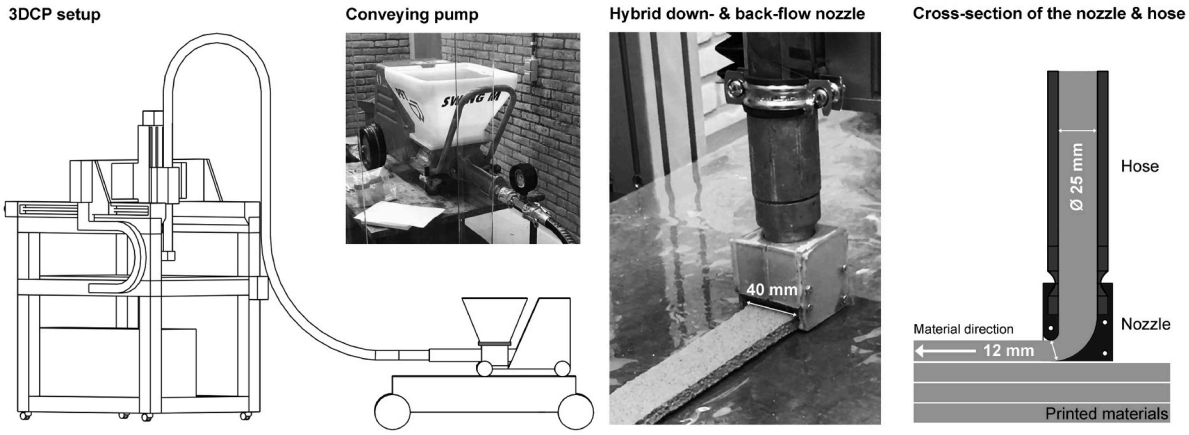

(a)

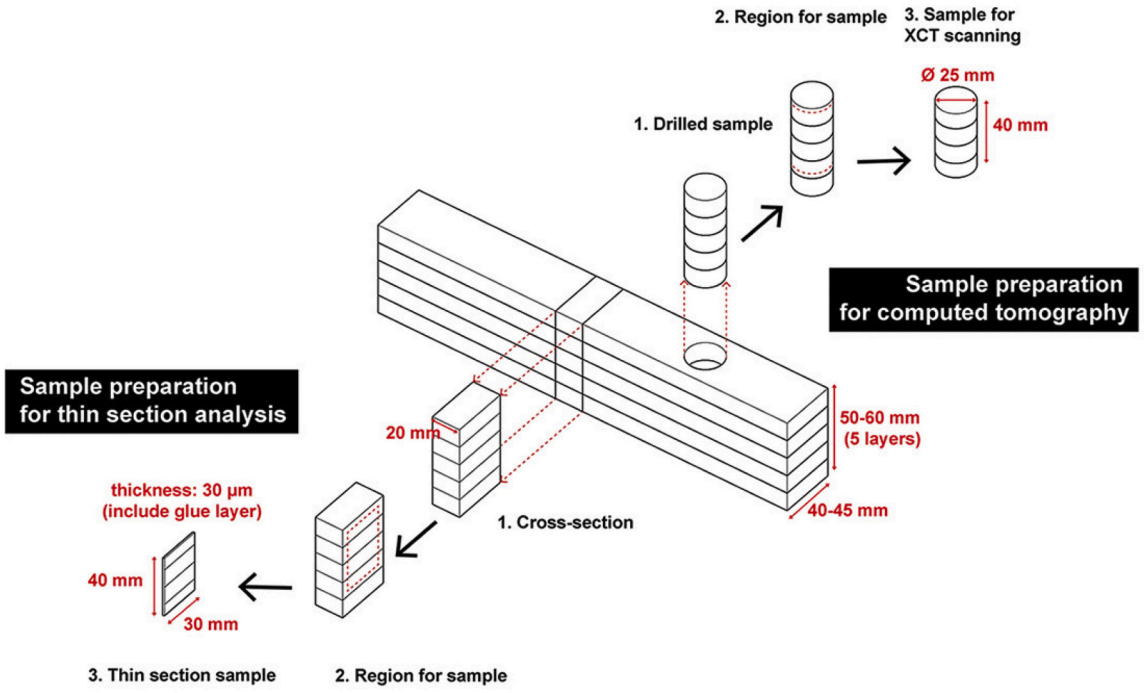

(b)

Fig. 1. (a) A lab-scale 3DCP setup (computer numerical control machine+conveying pump+nozzle); (b) Illustration of sample preparation for thin section analysis, and X-ray computed tomography.

Table 3
Mixing protocols for the fresh mixture preparation.

Time [min:s]	Procedures
-4:00	Mix dry materials at low speed (using a plenary HOBART mixer).
0:00	Add the liquid (water and SP) to the dry materials during mixing.
3:30	Pause, add VMA, and mix at low speed again.
7:00	Pause, scrape the walls and blade, and mix at high speed.
10:00	Stop, and deliver the fresh mixture to the hopper of the 3DCP setup.

2.3. Image acquisition and segmentation

2.3.1. Thin section

To capture images of entire thin sections, a digital film and photo scanner (Epson Perfection V800) with a resolution of up to 4800 dpi was used. A region of interest (ROI) (35 mm in length and 14.5 mm in width) was extracted from each scanned image for air void analysis (see Fig. 2). The resolution of scanned image was 7.2 μm/pixel. Thin sections were also studied with a Leica DM2500P optical microscope equipped with polarization and fluorescence capability. A Leica DFC310FX digital

Table 4
Printing parameters.

Printing start time (material age) [min]	Time interval between two layers [min]	Printing speed		Nozzle opening [mm^2]	Layer thickness [mm]	Nozzle standoff distance [mm]
		Material flow rate [L/min]	Nozzle moving speed [mm/min]			
15	1.5	1.7	3600	12 × 40	10–12	0

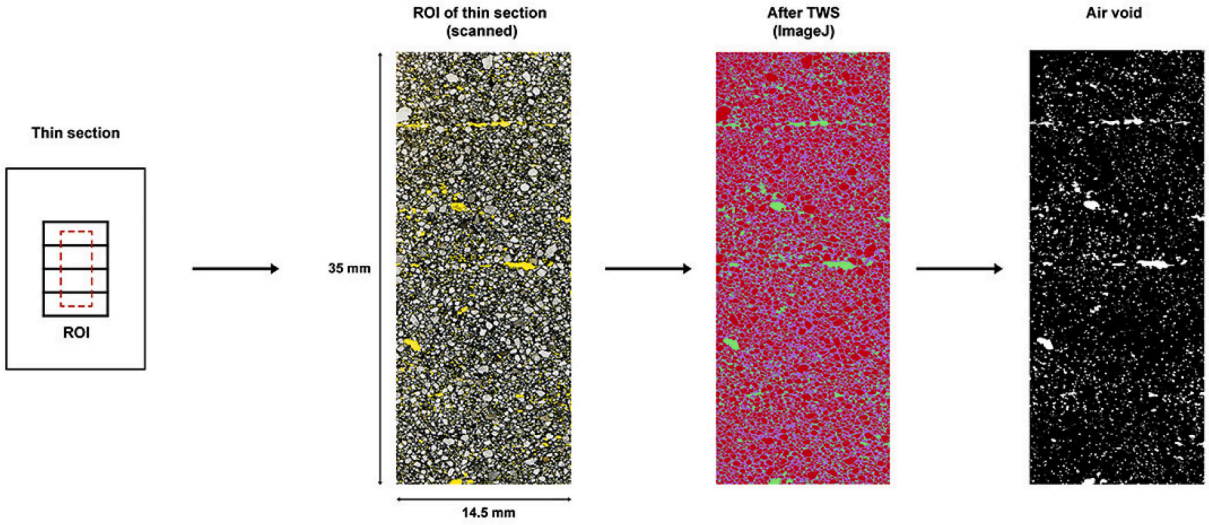

Fig. 2. ROI of the thin section and TWS segmentation process.

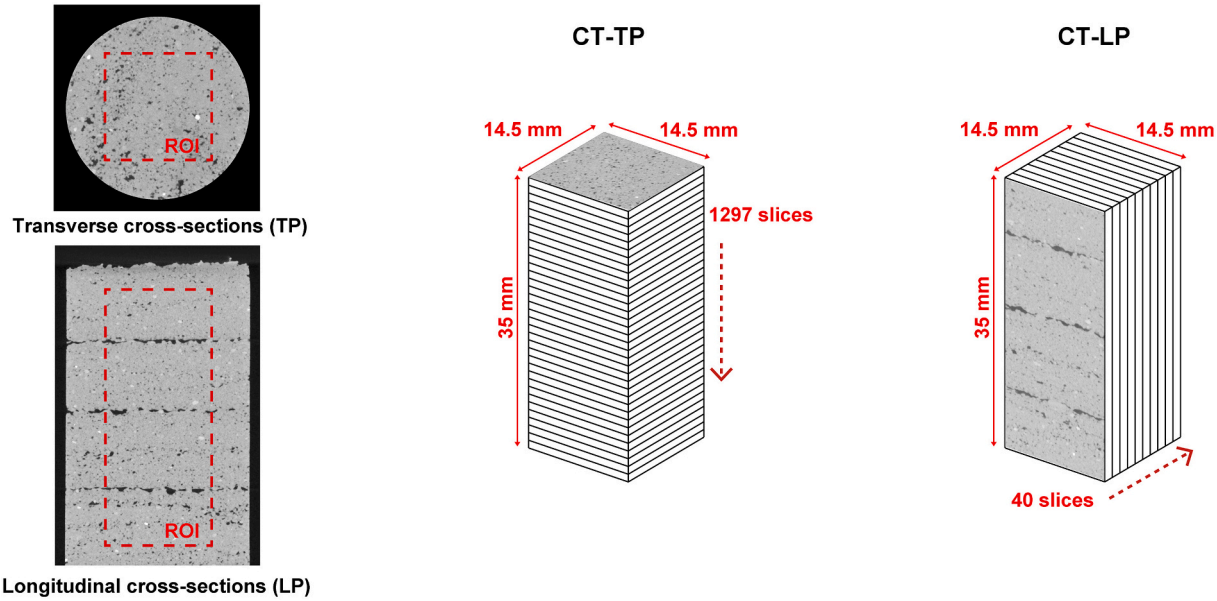

Fig. 3. CT-TP and CT-LP GSV images extracted from the reconstructed 3D volume.

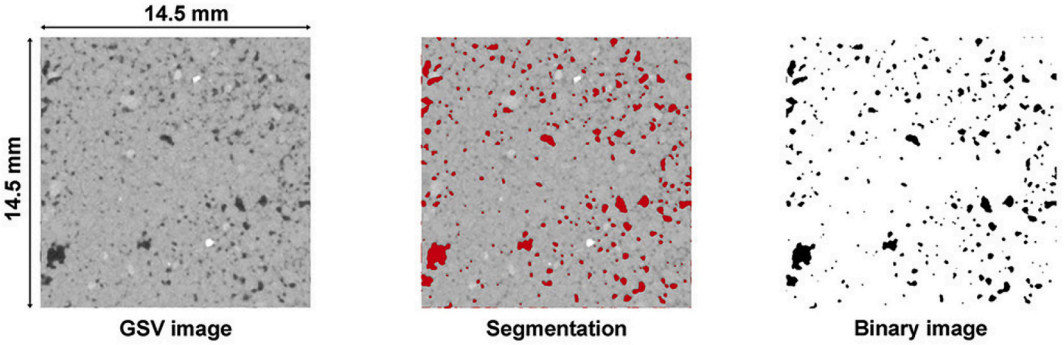

Fig. 4. An example of air void segmentation of GSV image.

Table 5
Overview of approaches for characterizing the air void system.

Image type	Optical image scanning - thin section	X-ray computed tomography	
	Longitudinal cross-sections (TS)	Longitudinal cross-sections (CT-LP)[a]	Transverse cross-sections (CT-TP)
Slice number (per sample)	1	40	1297
Resolution	7.2 μm/pixel	27 μm/pixel	27 μm/pixel
Air void content and distribution	P_{lp} V_{lp}	P_{lp} V_{lp}	P_{tp} V_{tp}
Air void size distribution	d_{2D}	d_{2D}	d_{3D}, Average d_{2D} (per slice)
Air void morphological study	Optical micrographs		3D visualization
Air void shape	2D circularity, 2D aspect ratio	2D circularity, 2D aspect ratio	Average 2D circularity (per slice)

[a] It is also possible to use all CT-LP images (537 slices) to reconstruct 3D volume for performing 3D analysis of air voids, which should generate the same results as using CT-TP images (V_{tp} and d_{3D}). However, the selected CT-LP images in this study were analyzed using the same means for processing TS images to provide more possibilities of the stereological examination.

camera was implanted in the optical microscope to acquire optical micrographs of the thin sections at 1392 × 1040 un-interpolated resolution. All acquired images were exported as uncompressed tagged image file formate (TIFF) images. The segmentation of air voids in scanned thin sections was carried out by Trainable Weka Segmentation (TWS) plugin from a freeware image processing software ImageJ [45]. The segmentation process via the method of TWS is illustrated in Fig. 2.

2.3.2. X-ray computed tomography

A Micro-CT scanner (Phoenix Nanotom) was used to obtain the microstructure of small cylindrical sample (diameter: 25 mm; height: 40 mm). By using the dedicated Phoenix Datos|x software, reconstructed slices were carried out. The resolution of obtained slices was 27 μm/pixel. For each sample, 1297 transverse planes/cross-sections (CT-TP) and 40 longitudinal planes (CT-LP) of grayscale value (GSV) images were obtained for performing image analysis (see Fig. 3).

ImageJ was also employed for conducting the image segmentation. However, instead of TWS, the thresholding method was employed to segment air voids in GSV images for saving computation time. An example of image segmentation result was illustrated in Fig. 4. For the image segmentation in this study, it should be noted that only the area of air voids larger than the resolution of images can be taken into account. Finally, the segmented binary images (only contained air voids) were acquired as the input of air void characterization.

2.4. Air void characterization

Air voids of 3D printed cementitious materials were investigated in terms of content, distribution, size, and shape. Different approaches to characterizing the air void systems were summarized in Table 5. Three aspects of air void characterization were presented as follows.

2.4.1. Content and distribution

For TS and CT-LP images (after segmentation), the air void content and distribution of each image were computed and analyzed via a MATLAB-code that was reported by Chen et al. [24]. Air void pixels were counted in every linear-row per image. The local porosity (P_{lp}) and air void content (V_{lp}) was calculated through Eq. (1) and Eq. (2), respectively.

$$P_{lp} = M_{row}/T_{row} \tag{1}$$

$$V_{lp} = M_{image}/T_{image} \tag{2}$$

where M_{row} is the pixel number of air void per row, and T_{row} represents the total pixel number per row. M_{image} and T_{image} stand for the pixel number of air void and total pixel number per image, respectively. In the case of CT-TP images, the local porosity (P_{tp}) that was equal to air void content of each transverse slice can be computed via Eq. (3). For calculating air voids content (V_{tp}), Eq. (4) was used.

$$P_{tp} = M_{image}/T_{image} \tag{3}$$

$$V_{tp} = V_{air}/V_{total} \tag{4}$$

where V_{air} is the total air volume of ROI prism, and V_{total} is the volume of ROI prism. The air void volume was measured by using 3D Objects Counter plugin from ImageJ.

2.4.2. Size distribution

For some 3D printed cementitious materials with weak interlayer bondings, it has been found that the air voids in the interface region exhibited a larger average size than that of other regions [42]. The coarse pore probably induced by merging and overlapping of entrapped air voids could weaken the mechanical performance of printed structure significantly. Thus, it is necessary to quantify the air void size distribution in this context. The area of each pore in TS and CT-LP images and the volume of each pore in the reconstructed 3D volume using CT-TP images were determined by Analyze Particles and 3D Objects Counter (ImageJ), respectively. The pore diameter was generally used to describe the pore size. 2D and 3D pore diameter (d_{2D}, d_{3D}) could be computed via Eq. (5, 6), respectively.

$$d_{2D} = \sqrt{4Area/\pi} \tag{5}$$

$$d_{3D} = \sqrt[3]{6Volume/\pi} \tag{6}$$

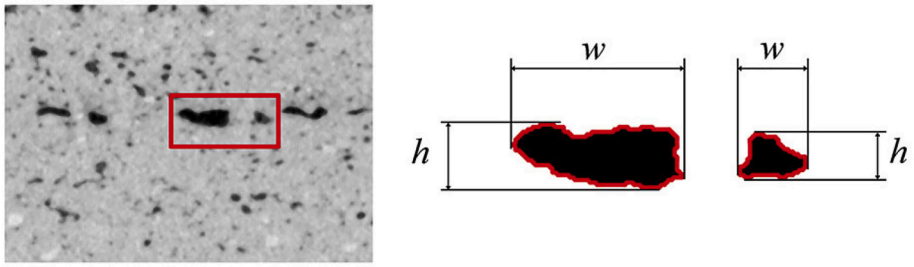

Fig. 5. Illustration of the horizontal width and vertical height of the air void.

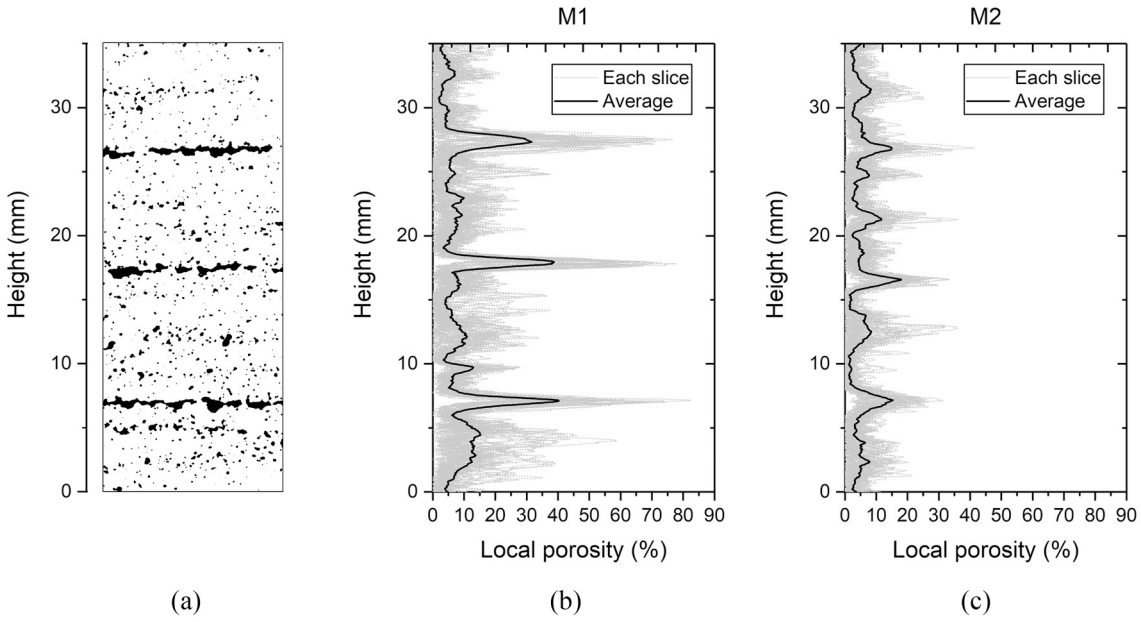

Fig. 6. Local porosity vs. sample height of samples M1 and M2 based on 40 CT-LP images: (a) An example of CT-LP image (after segmentation); (b) Result of sample M1; (c) Result of sample M2. The grey line is the computed result of each slice, and the black curve means the average result from 40 slices.

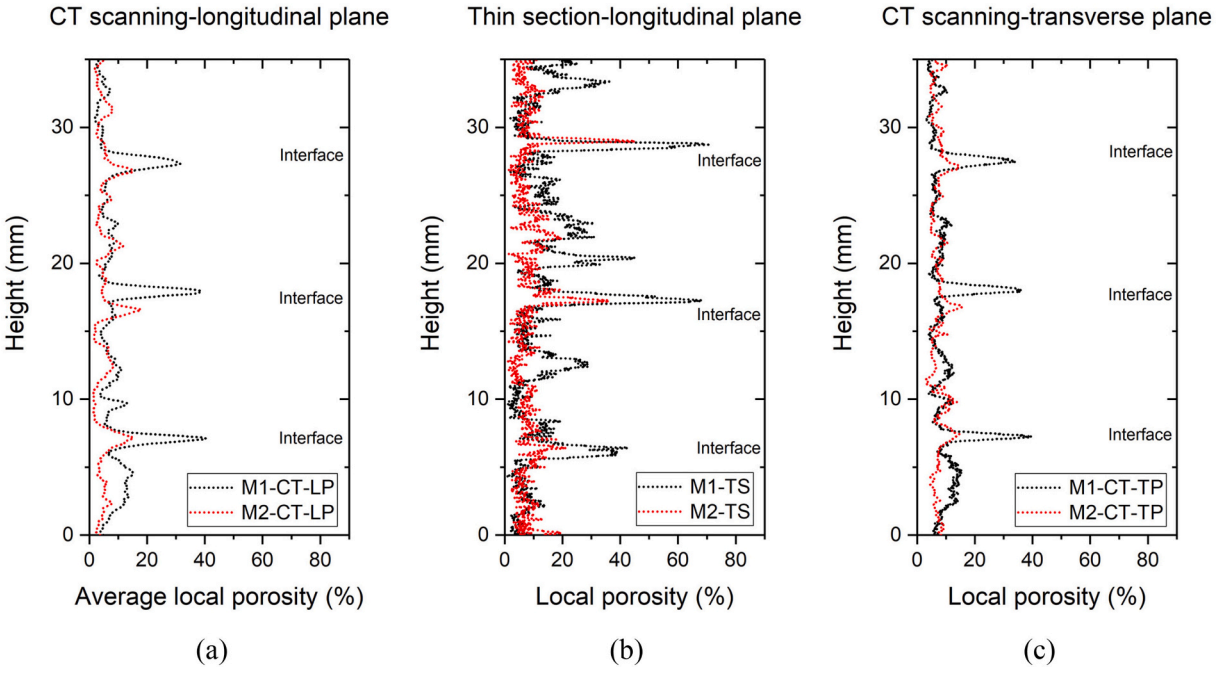

Fig. 7. Local porosity vs. sample height of samples M1 and M2: (a) Average result of CT-LP images; (b) Result of TS images; (c) Result of CT-TP images.

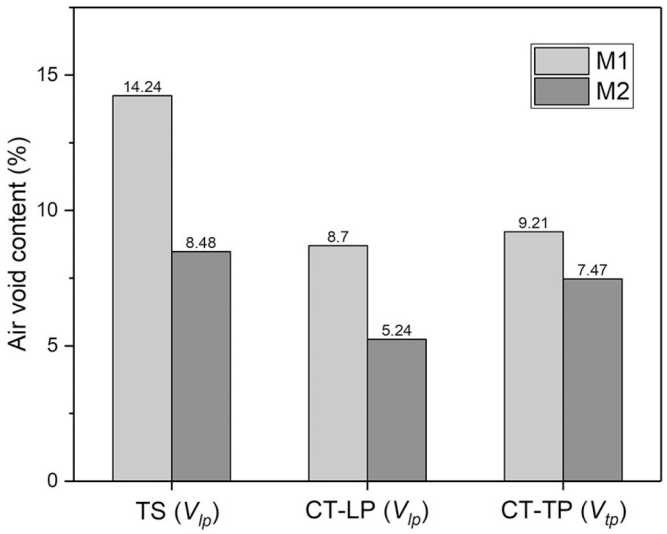

Fig. 8. Total air void content V_{lp} from TS images (left); Total air void content V_{lp} from CT-LP images (middle); Total air void content V_{tp} from CT-TP images (right).

Besides, to characterize the pore size along with the sample height, the average 2D air void diameter of every CT-TP image was calculated as well.

2.4.3. Shape property

The morphology of air voids was observed on optical micrographs of thin sections and visualized in 3D through using CT-TP images. This is a qualitative way to illustrate the distribution and shape of air voids. Furthermore, 2D circularity and 2D aspect ratio of each pore, as given in Eq. (7) and Eq. (8), were used to quantify the shape properties of air voids in TS and CT-LP images from Section 2.3. The shape of air voids is close to a perfect circle when the value of circularity is about 1. Elongated/concave pores appeared in the interface area can be directly observed in longitudinal cross-sections of printed samples (see Fig. 5). The aspect ratio was employed to evaluate the elongation magnitude of the pore structure.

$$Circularity = 4\pi\left(A/S^2\right) \tag{7}$$

$$Aspect\ ratio = w/h \tag{8}$$

where A, S, w, and h are the area, perimeter, horizontal width, and vertical height of an air void.

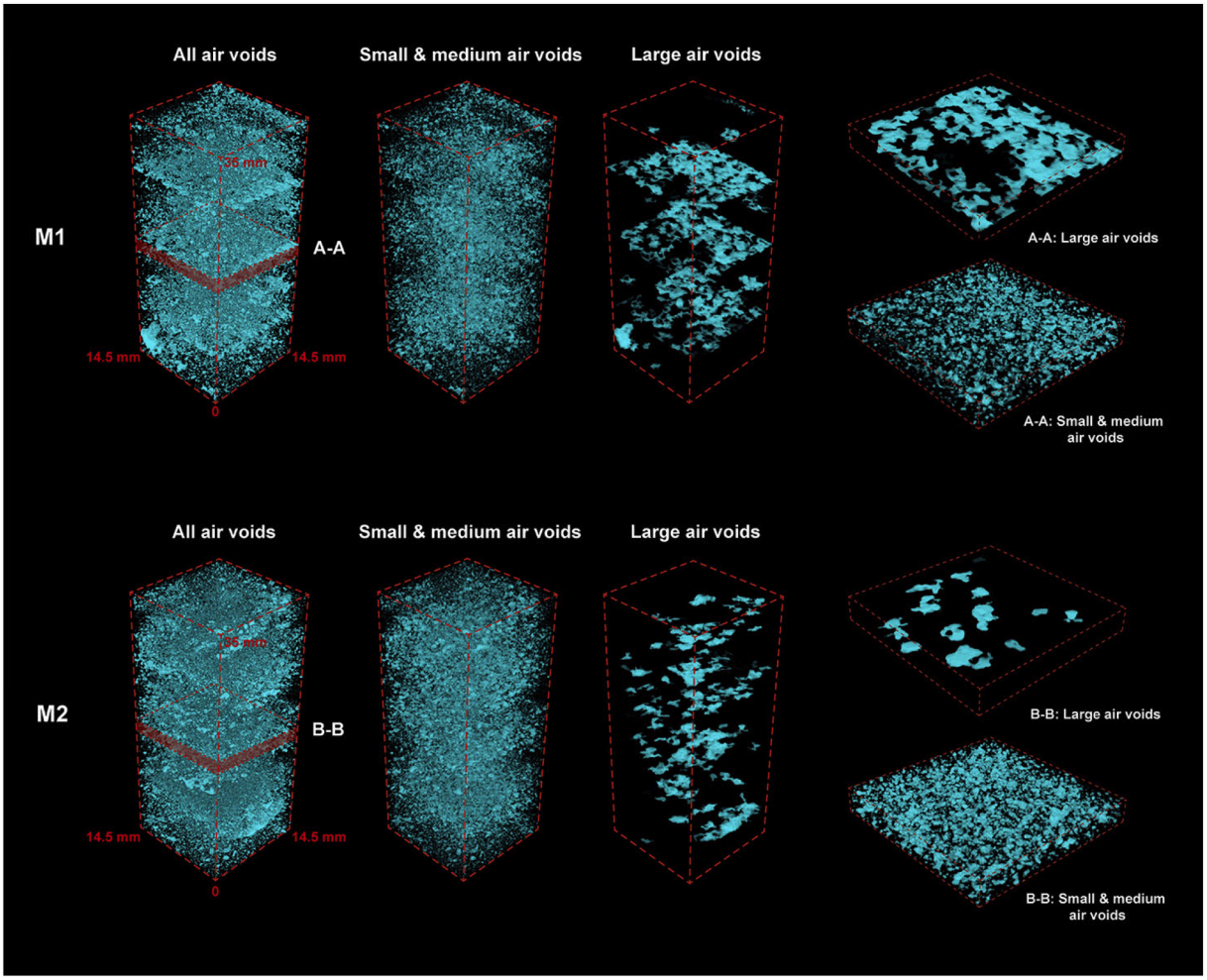

Fig. 9. 3D visualization of the air voids in the prism ROI. A-A section: interface region of sample M1 (thickness: 2 mm); B-B section: interface region of sample M2 (thickness: 2 mm). Small & medium air voids: 10–1000 μm; Large air voids: 1000–6000 μm.

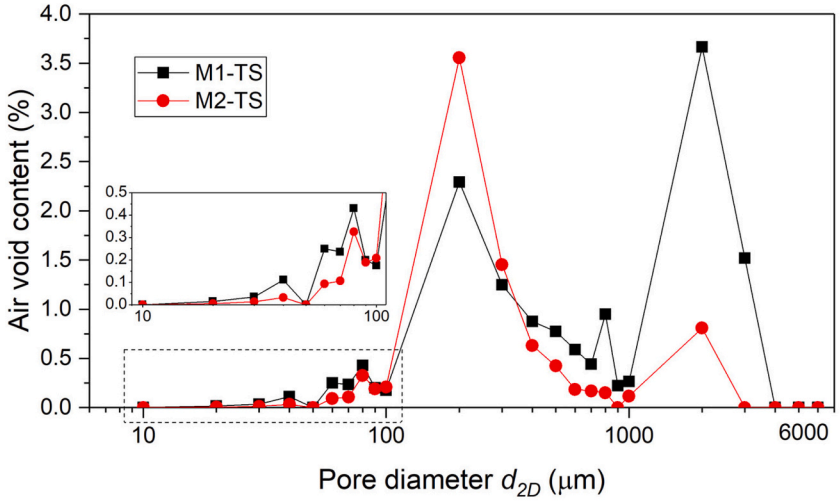

(a)

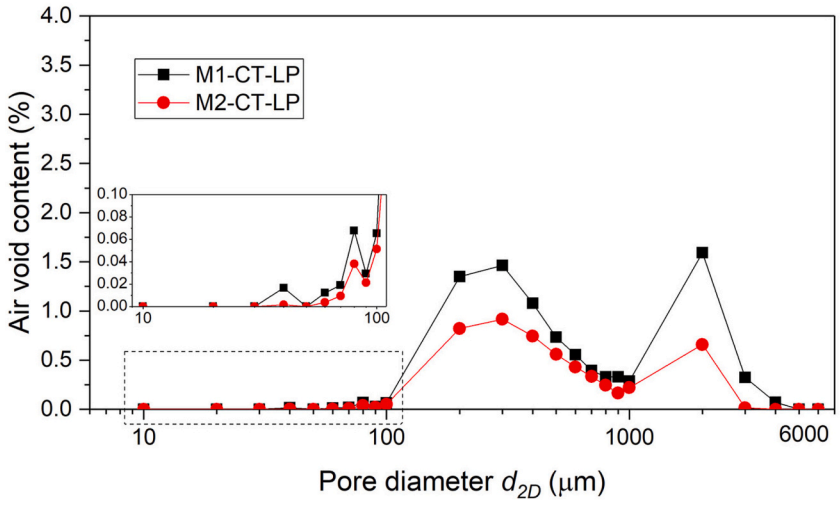

(b)

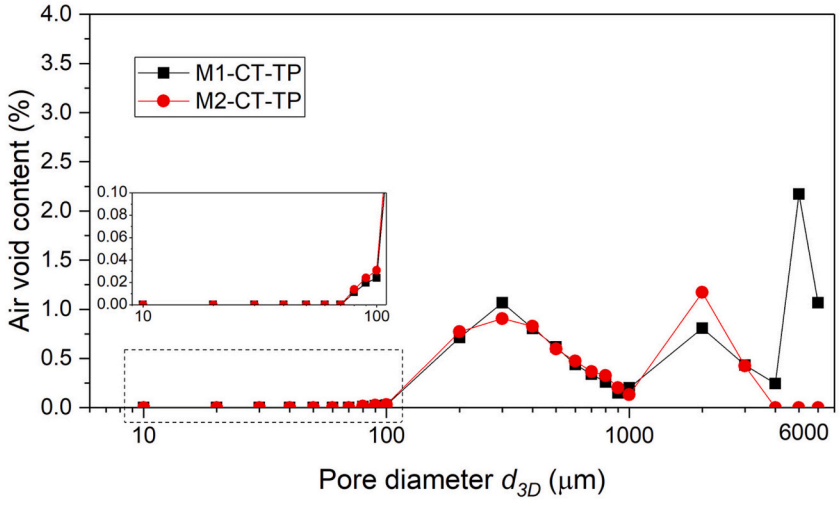

(c)

Fig. 10. Pore size distribution of samples M1 and M2: (a) d_{2D} from TS images; (b) d_{2D} from CT-LP images; (c) d_{3D} from CT-TP images; (d) Characterized into three pore size groups.

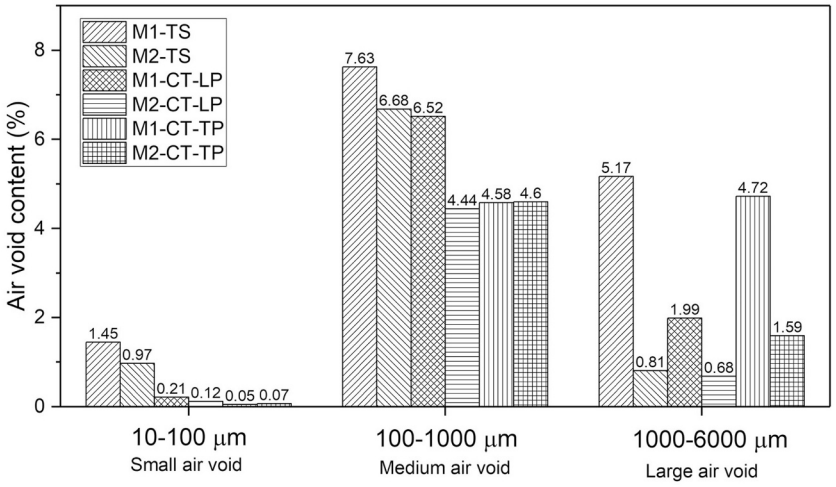

(d)

Fig. 10. (*continued*).

3. Results and discussion

3.1. Air void content and distribution

Based on the CT-LP images, the local porosity of samples M1 and M2 is illustrated in Fig. 6. Additionally, Fig. 7 shows the local porosity results obtained by TS, CT-LP, and CT-TP images. In general, the air voids were not homogeneously distributed within samples M1 and M2. It could be found that the interface of the printed samples displayed relatively higher air void content compared to other regions, especially sample M1. The position of interface areas could be indicated in Fig. 7. In comparison with sample M2, sample M1 exhibited much higher air void content in the interface, which agreed with the previous study of the authors [42]. Magnitude differences of the local porosity results were also observed across measurements. It can be found that less significant differences between CT-TP and CT-LP images compared with that between CT-TP and TS images. As mentioned earlier, the resolution of scanned thin sections is about 7.2 μm/pixel, which is much smaller than that of GSV images (27 μm/pixel) from CT scanning (CT-LP and CT-TP images). Thus, small air bubbles with a theoretical diameter between 7.2 μm and 27 μm were also taken into account in TS images. Additionally, using different image segmentation methods may induce changes in porosity as well.

The results of total air void contents computed by using different images are reported in Fig. 8. Sample M1 shows a higher void content than sample M2. However, notable differences in the total air void content obtained by using different methods were also found in Fig. 8. In comparison with the air void content obtained from CT-TP images, a much higher air void content was predicted by TS images, and a slightly lower result was achieved by CT-LP images. Due to the 2D effects, the results measured via TS and CT-LP images may lead to the over−/under-estimation of air void content compared with CT-TP images. Besides, the above-mentioned differences between TS and CT images could also contribute to such deviations.

3.2. Air void size distribution

The CT-TP images for each sample are visualized in 3D, as shown in Fig. 9. The cyan colored objects in the image represent the air voids within the sample. The air voids were segmented into two groups based on the pore diameter in CT-TP images (d_{3D} of small and medium air voids: 10–1000 μm; d_{3D} of large air void: 1000–6000 μm). As shown in

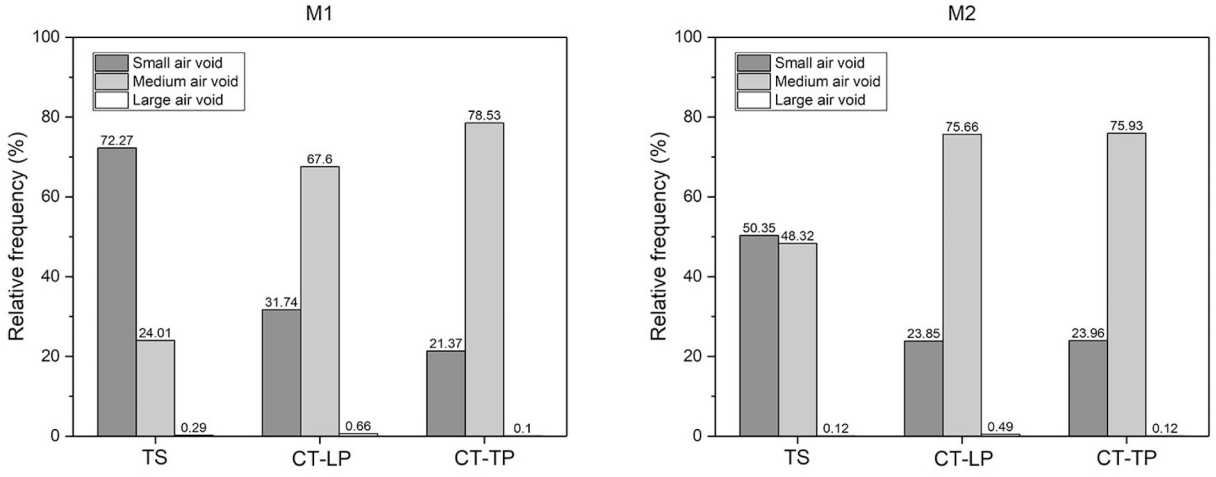

Fig. 11. Relative frequency of air voids in three pore size groups characterized by analyzing TS, CT-LP and CT-TP images: (a) Sample M1; (b) Sample M2.

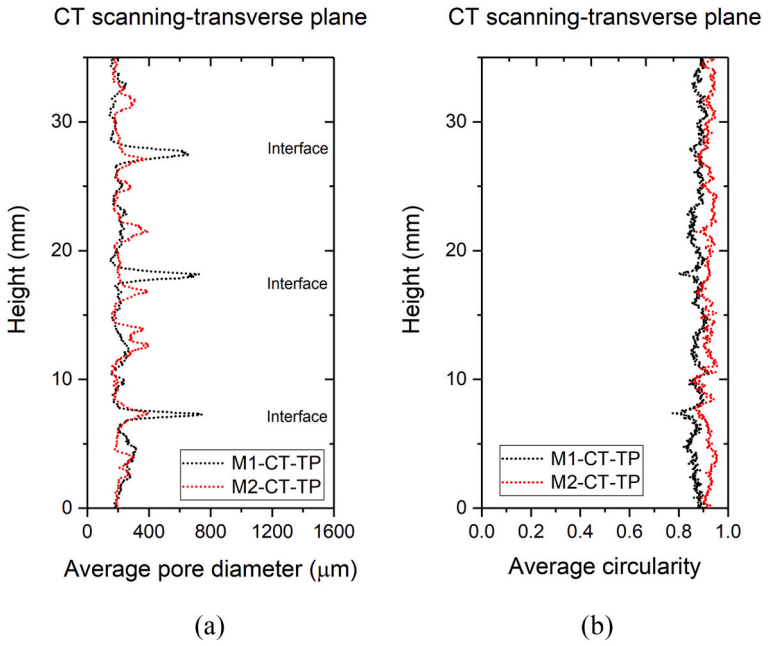

Fig. 12. (a) The average pore diameter of air voids in each CT-TP image from the bottom to the top of the sample; (b) The average circularity of air voids in each CT-TP image from the bottom to the top of the sample.

Fig. 9, most of the pores in both samples belong to small and medium air voids. The large air voids in sample M1 were mainly distributed in the interface area, whereas a relatively uniform distribution of large air voids throughout the sample was found in sample M2. Rationally, the concentrated pores in the interface area led to the high local porosity (see Fig. 7). Besides, Fig. 12 (a) presents the average pore diameter of air voids in each transverse cross-section from the bottom to the top of the sample. Particularly in sample M2, coarser air voids that could result in the high average pore diameter were also indicated in the layer region.

Fig. 10 presents the pore diameter distribution of samples M1 and M2. In general, the medium air voids (100–1000 μm) accounted for the highest void content across measurements. Sample M1 exhibited a higher volume of large air voids (1000–6000 μm) than sample M2. The relative frequency of air voids in different size groups is illustrated in Fig. 11. Magnitude differences of the results between TS and CT (LP and TP) images could be indicated. As shown in Fig. 11, small air voids (10–100 μm) possessed the largest relative frequency of overall air voids in the results obtained from TS images. However, for CT-LP and CT-TP images, most of air voids were characterized as medium air voids. As mentioned in Section 3.1., the differences between TS and CT (-LP and -TP) images in the image resolution and the segmentation method may induce this phenomenon.

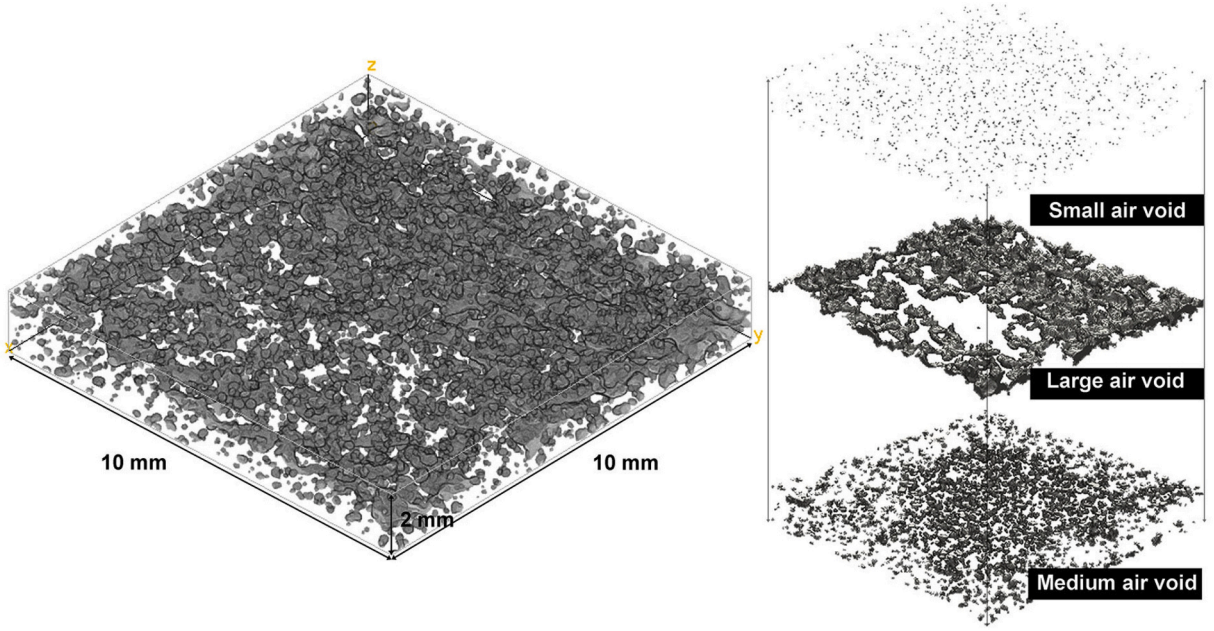

Fig. 13. 3D configuration of the interlayer region in sample M1 (volume: 10 × 10 × 2 mm^3).

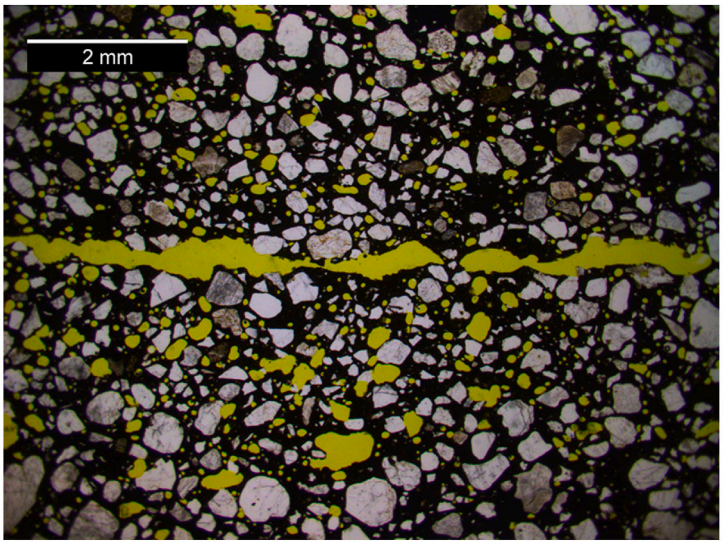

(a)

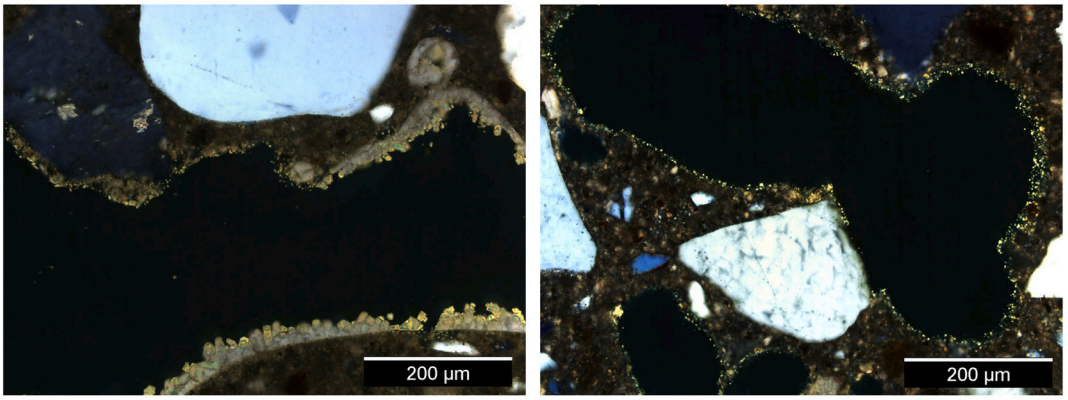

(b) (c)

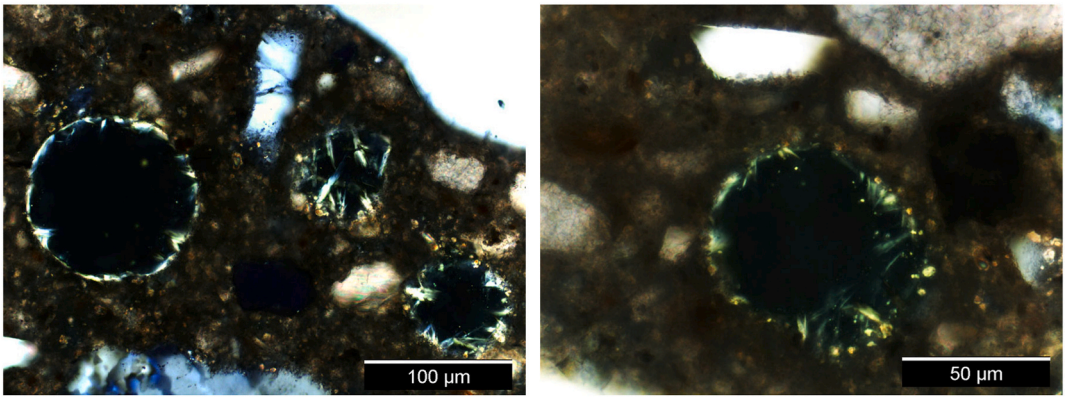

(d) (e)

Fig. 14. (a) Photomicrograph of the interlayer region in sample M1 (under PPL mode). Yellow areas represent the air bubbles. Image fields: 8.95 × 6.69 mm^2; (b) Photomicrograph of the large air void (part) in the interface (under XPL mode). Image fields: 0.70 × 0.53 mm^2; (c) Photomicrograph of the medium air void (under XPL mode). Image fields: 0.70 × 0.53 mm^2; (d) Photomicrograph of the small air void (under XPL mode). Image fields: 0.35 × 0.27 mm^2; (d) Photomicrograph of the small air void (detail) (under XPL mode). Image fields: 0.18 × 0.14 mm^2. (For interpretation of the references to color in this figure legend, the reader is referred to the web version of this article.)

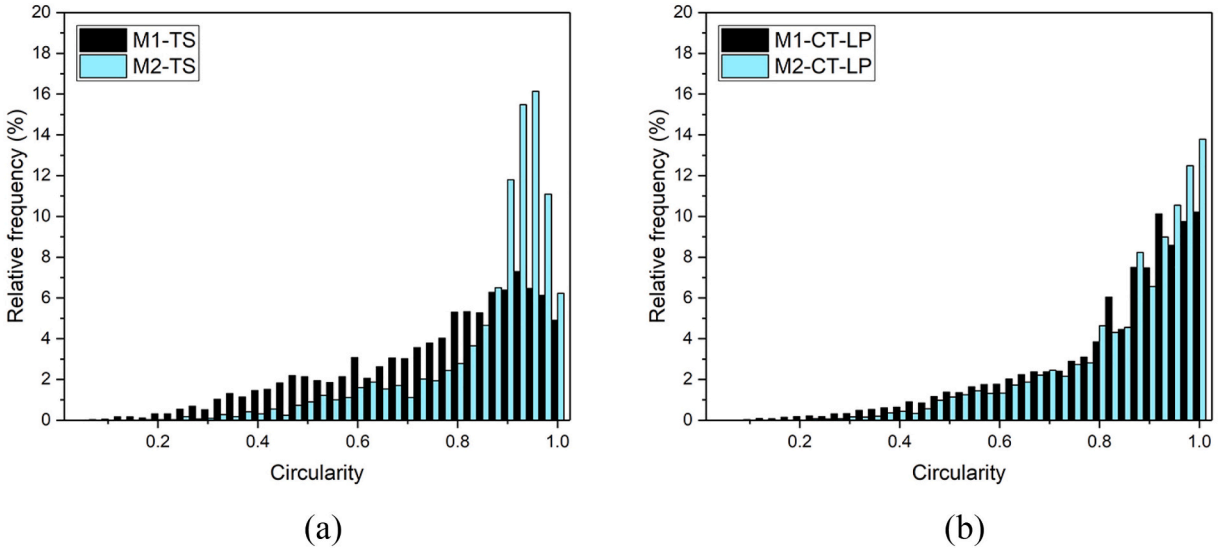

Fig. 15. Circularity distribution of air voids measured by: (a) TS images; (b) CT-LP images.

3.3. Air void shape property

3.3.1. Morphological study

In Fig. 9, large air voids were mainly found in the interlayer region of sample M1. A typical example of the 3D configuration of air voids in the interface region of sample M1 (part of A-A section) is presented in Fig. 13. The connectivity of large air voids in the interlayer was evidently observed. The vast majority of medium and large air voids exhibited irregular and anisotropic shapes, which agreed well with the findings of Van Der Putten et al. [46]. In Fig. 14 (a), a typical interface area of the printed sample (M1) is highlighted. Under plane polarized light (PPL) mode, epoxy impregnated air voids display yellow color because of the fluorescent pigment. In contrast, the binder appears black, and the sand particles are bright with light grey- and/or brown-textures. Similar to the 3D configuration of the air void system, large air voids with the elongated shape were found in the interface area.

Photomicrographs of large air voids (Fig. 14 (b)), medium air voids (Fig. 14 (c)), as well as small air voids (Fig. 14 (d, e)) were acquired under crossed polarized light (XPL) mode to observe these air voids in thin sections further. The large air void appears to act as a 'crack' between two layers, whereas the medium air void may be formed by several connected ellipsoidal pores. Small air void as the minimum unit could keep the round shape in the paste. In Fig. 14 (b–e), it can be seen that all air voids were filled with crystals, most likely portlandite and/or calcite (see Fig. 14 (b)). Needle-like ettringite or portlandite crystals were observed on the surface of small air voids, as seen in Fig. 14 (d, e).

3.3.2. Circularity and aspect ratio

Fig. 15 illustrates the comparison of the air void circularity distribution of different specimens, where the air void circularity distributions were obtained from TS and CT-LP images, respectively. The y-axis in Fig. 15 presents the relative frequency of the pore circularity for describing the shape property of air voids in different specimens. For each measurement, the general trend of the pore circularity distributions was similar in different specimens. Compared with sample M1, there is a higher amount of air voids with the higher values of circularity (0.9–1) in sample M2. Variations across measurements were also evident. The circularity of the maximum relative frequency, as obtained from TS images, is around 0.925–0.95, whereas this value is 1 in CT-LP images. In Fig. 12 (b), the average air void circularity in transverse cross-sections of sample M2 is slightly larger than that of sample M1 throughout the specimen. The correlation between the average circularity and the pore size is illustrated in Fig. 16. For both samples, air voids with the small pore size showed the relatively higher average value of circularity.

The aspect ratio was also studied to investigate the orientation of air voids in the horizontal direction. Fig. 17 illustrates the aspect ratio of air voids throughout the sample based on TS and CT-LP images. Compared with TS images (Fig. 17 (a)), the results obtained by CT-LP images could indicate the approximate interface position in Fig. 17 (b). Especially in sample M1, many air voids with large aspect ratio ($w/h > 3$) were found at the sample height of about 7.2 mm, 18.1 mm, and 27.4 mm, where the high local porosity appeared in sample M1, as shown in Fig. 7. The aspect ratio distribution of air voids is demonstrated in Fig. 18. The general trend of aspect ratio distribution is the same for different samples by using different types of images. For both samples M1 and M2, more than 35% of air voids are in the range of 1.1–8. The aspect ratio in the range of 1.1–2 represents the largest category (except the results of CT-LP images in sample M2). In Fig. 19, the relationship between the average aspect ratio and the pore size is reported. The average aspect ratio of small air voids in both samples was close to 1. For medium and large air voids, the aspect ratio exhibited an increasing trend with the increase of pore diameter, which was clearly indicated in Fig. 19 (b). Note that, owing to the limited image resolution, especially the images obtained using X-ray computed tomography, many small air voids comprise only several pixels (in 2D), which may be insufficient to indicate their intrinsic shape properties. Thus, most of small air voids appear to be more spherical than macropores.

3.4. Perspective and limitations

3.4.1. Formation of air voids in printed cementitious materials

Overall, the air voids in 3D printed cementitious materials showed significant differences in morphology and distribution compared with mold-cast cementitious materials in [35–37]. It could be found that small and medium air voids (10–1000 μm) were primarily distributed in the printed layer, whereas most of the large air voids (1000–6000 μm) appeared in the interlayer region. Since air-entraining agents were not added in the studied mixtures, the formation of small air voids (10–100 μm) was possibly due to the existence of grinding aid that was used for producing Portland cement. Besides, the presence of polycarboxylate ether-based superplasticizer in mixtures may also contribute to the entrainment of such air voids [47,48].

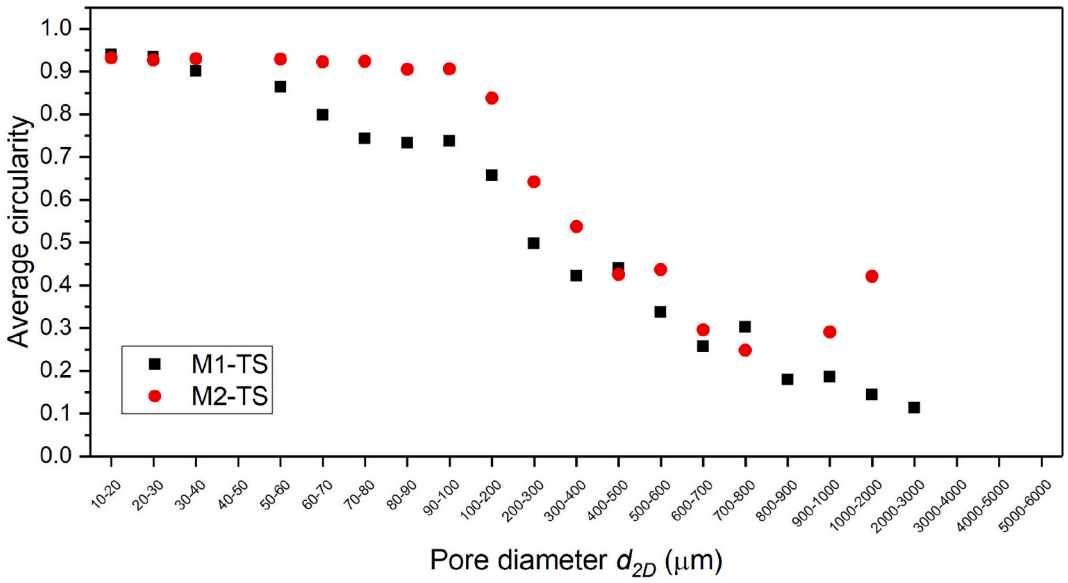

(a)

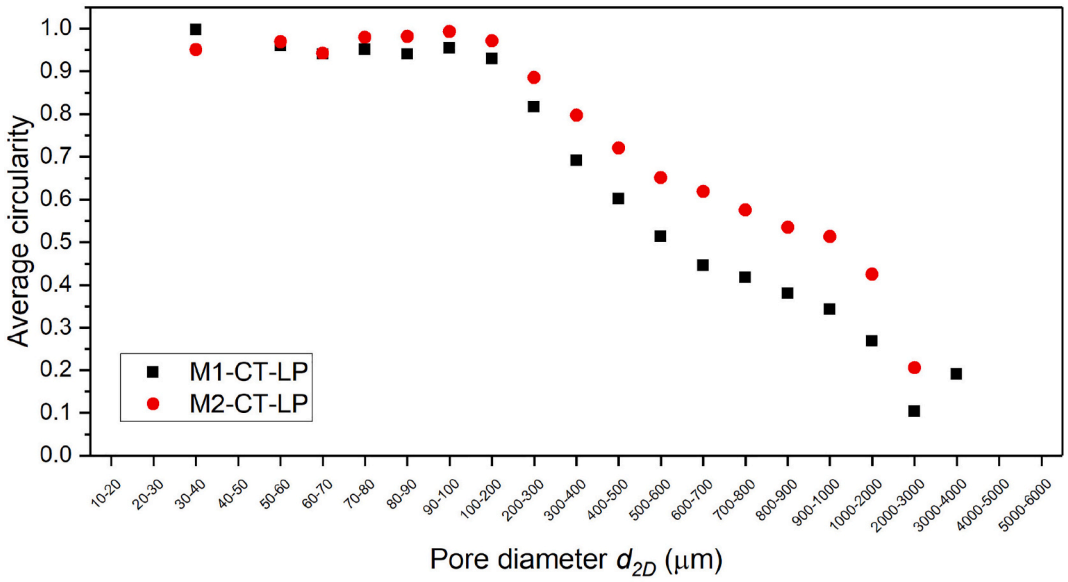

(b)

Fig. 16. Correlation between average circularity and pore size of samples M1 and M2: (a) TS images; (b) CT-LP images.

The fresh mixtures (both M1 and M2) displayed very high consistency during the extrusion process, as well as high stiffness and near zero-slump after deposition. Due to the high flow consistency of fresh mixtures, air bubbles were stabilized and may be evenly distributed in the matrix during the mixing process of fresh mixture preparation. Afterwards, the fresh mixture was extruded through a conveying pump. The extrusion force provided by the pump can compact the fresh mixture, which could also redistribute and reshape the air voids in the filament. Besides, the loading from upper layers seemed to compress/compact air voids in the substrate vertically. As a consequence, massive compressed, merged, and overlapped air voids with the elongated shape that showed a high value of aspect ratio in the longitudinal cross-section eventually were found in the layer regions (see Fig. 14 (a, c)). Under the extrusion pressure, the small air voids were also difficult to retain the spherical shape. Most of them displayed slight anisotropy in the 2D image (Fig. 14 (a)) and ellipsoid shape in the 3D visualization (Fig. 13). It should be noted that coarse air voids may be enclosed in the filament during the extruding/printing process since the vacuum de-airing system was not adopted in our extrusion system. Few large air voids were recognized in the layer of both samples M1 and M2 (see Fig. 9).

The large air void was formed mainly in the interface area, which can be attributed to the layer-wise manufacturing process in 3DCP. Many parameters, e.g., material thixotropy, time gaps, nozzle types, and others, influenced air voids content in the interlayer region from studies [22–24]. In this study, the printing parameters were kept identical. The only difference between the two studied mixtures was the proportions of HGCC and LGCC in calcined clay. Sample M2 containing a lower content of HGCC, showed much lower porosity in the interface region in comparison with sample M1. Chen et al. [42] reported that increasing the content of HGCC in calcined clay could enhance buildability and

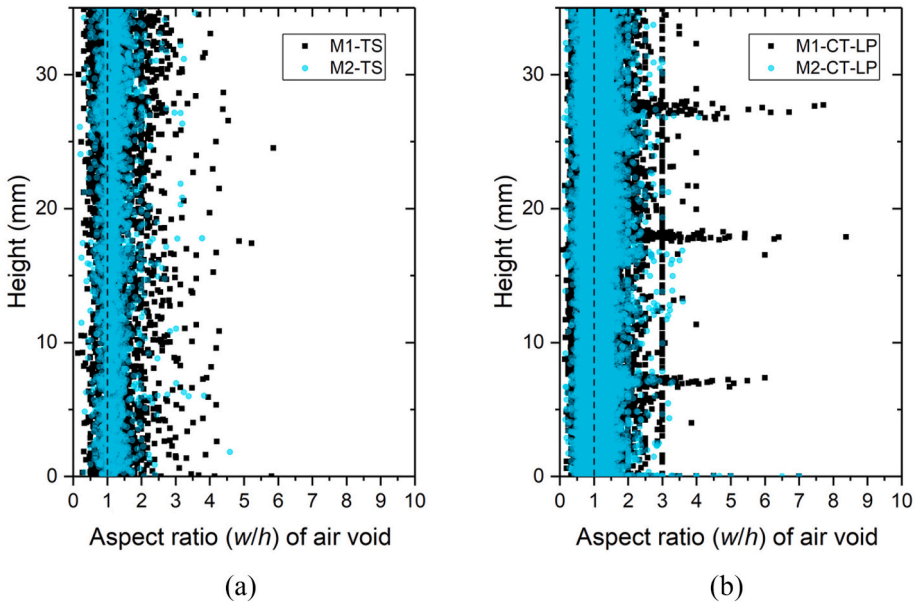

Fig. 17. The aspect ratio of air void along with the sample height: (a) TS images; (b) CT-LP images.

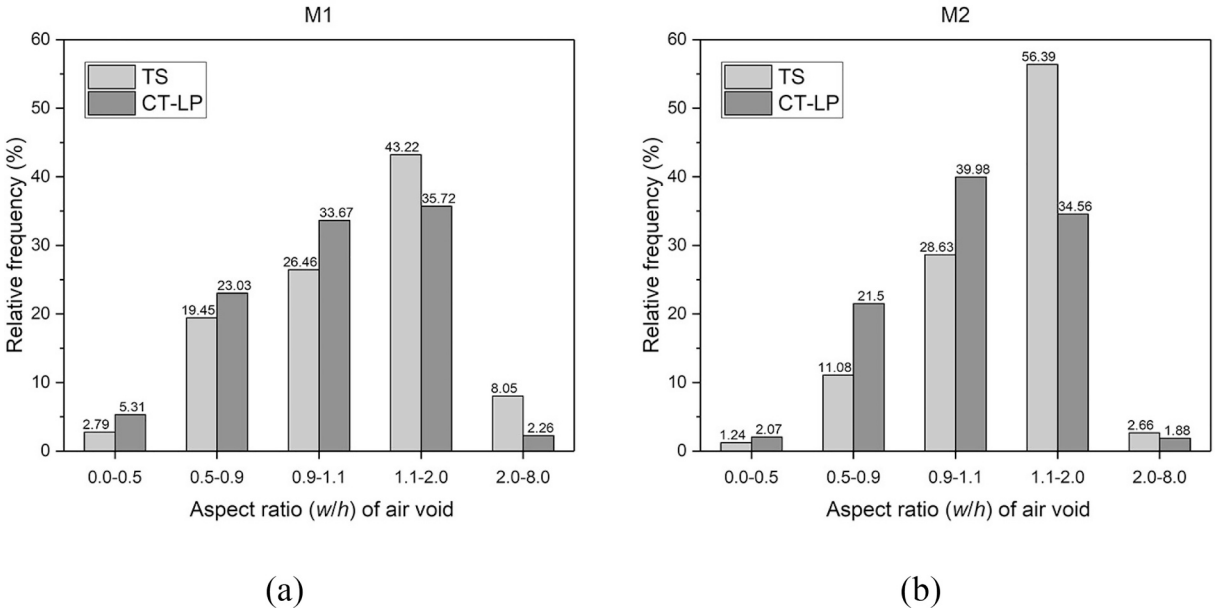

Fig. 18. The aspect ratio distribution of air voids measured by using TS and CT-LP images: (a) Sample M1; (b) Sample M2.

structural build-up behavior at rest of fresh mixtures for 3D printing. This is probably due to the enhancement of particle flocculation and increased water adsorption induced by HGCC. Under the identical printing parameters, mixture M1 exhibited better buildability than mixture M2 (see Fig. 20). However, the fresh mixture with the higher thixotropy/buildability seems to enclose more large air voids in the interface. As mentioned by Roussel [21], the higher the thixotropy of the fresh mixture, the weaker the intermixing between layers. Without the sufficient intermixing and contact areas between layers, longitudinal cavities (air voids with the elongated shape) would be formed. This may explain why the sample M1 exhibited a higher amount of air voids in the interface than sample M2. Furthermore, as shown in Fig. 21, printed sample M2 showed the superior 28 days compressive strength in three test directions compared to printed sample M1. The results agreed that the hardened cementitious materials with a higher air void content exhibited weak compressive strength.

3.4.2. Comparison between optical image scanning and X-ray computed tomography

The comparison between optical image scanning and X-ray computed tomography in terms of sample preparation, image acquisition, and the pros and cons is summarized in Table 6. The main challenge of using thin sections to characterize air void system of printed samples is the sample preparation, which is not only a time-consuming process but also a delicate work. Unlike thin sections, the cored sample in this study for CT scanning can be prepared easily. However, the accuracy of digital image analysis is mostly dependent on the resolution of images. As mentioned by studies [39,49], maximum resolution of GSV

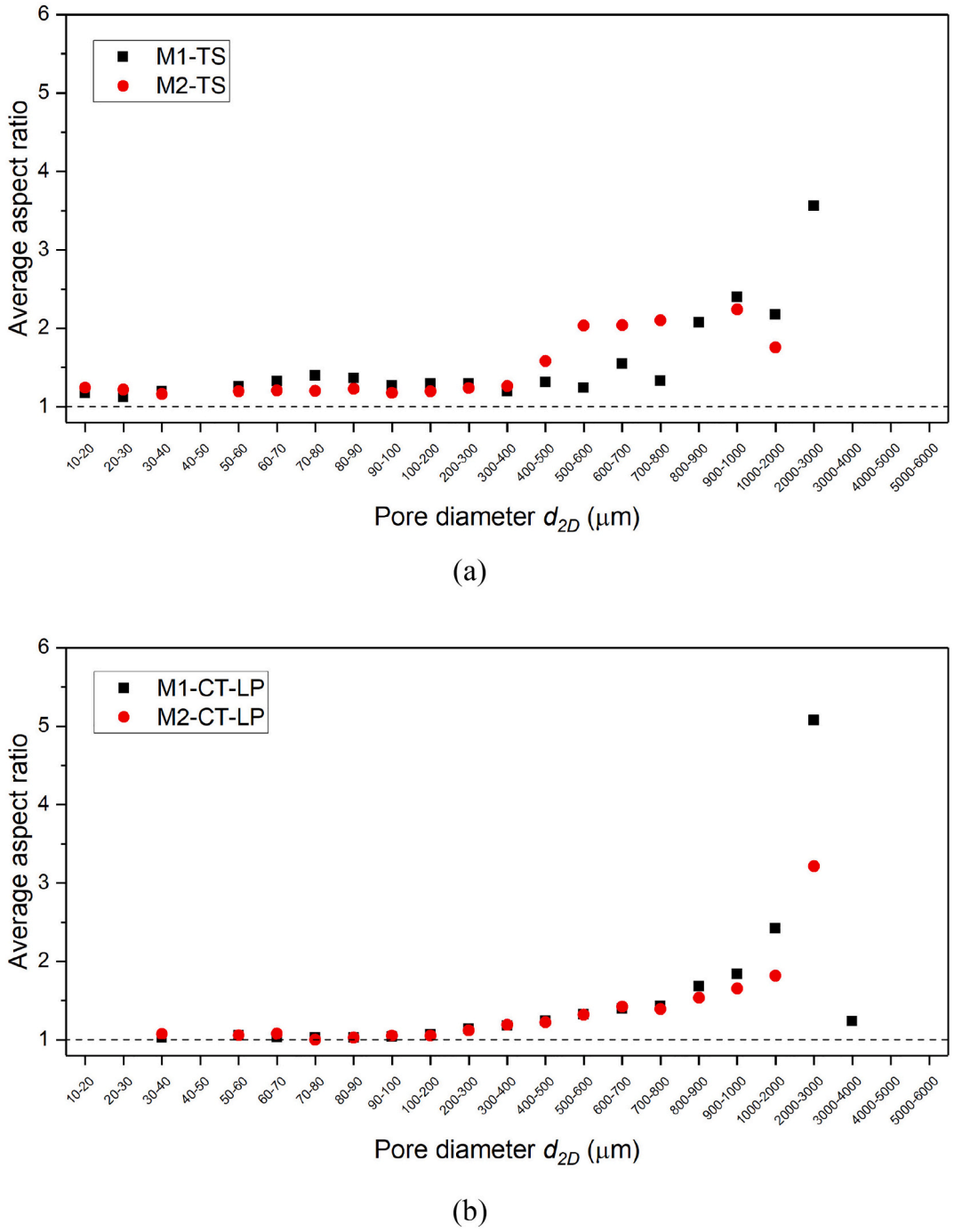

Fig. 19. Correlation between average aspect ratio and pore size of samples M1 and M2: (a) TS images; (b) CT-LP images.

images from CT scanning is limited by the dimension of the sample. The cored sample should be equal in size or larger than the necessary representative elementary volume. In contrast, it is apparently in contradiction with the fact that the resolution of 10 μm is needed to quantify the small air voids. In further research, multiscale samples might be used to conduct the air void characterization via CT scanning.

In comparison with CT-TP images, the limitations of using TS and CT-LP images on air void characterization should be highlighted. First, as mentioned earlier, using TS and CT-LP images may over−/under-estimated the total air void content and the local porosity along with the longitudinal cross-section of printed samples due to the 2D effects. Second, the acquired pore area in the TS and CT-LP images may not represent the actual size of air voids, which depends on the position of the cross-section (see Fig. 22). Finally, most of the air voids in printed samples displayed elongated/concave shapes. The analysis of TS and CT-LP images can indicate the shape properties of air voids in one plane projection. In contrast, it is difficult to reveal the spatial anisotropy/heterogeneity of air voids. For further study, it is recommended to increase the dimension of the printed sample for optical microscopy/scanning. As described by ASTM C457–98 [29] and NEN-EN 480–11 [50], the concrete specimen with a field area of 100 × 100 mm^2 was required for performing air void analysis. The large specimen may require longer preparation time (e.g., cutting, polishing, and other treatments) and lead to a reduction of image resolution. In contrast, it can offer more interface regions for studying and quantifying the large air voids (>1000 μm).

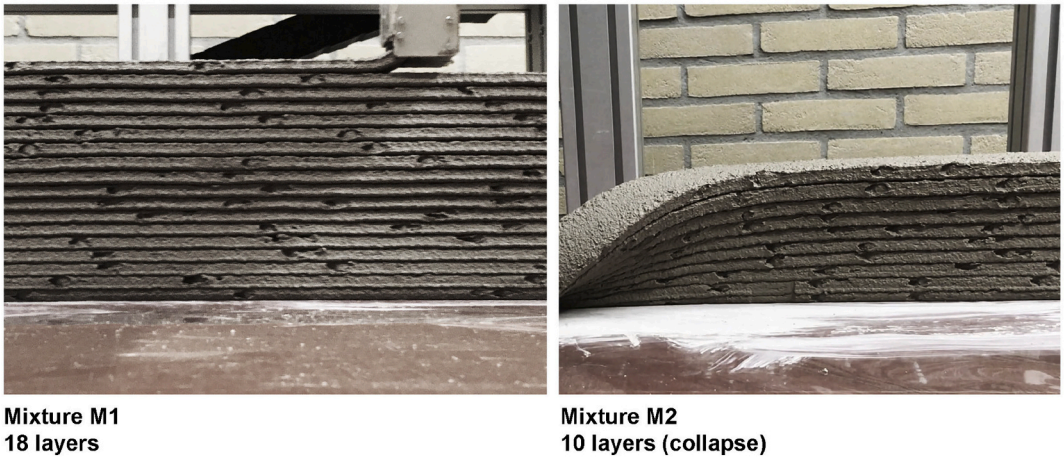

Fig. 20. Buildability test results.

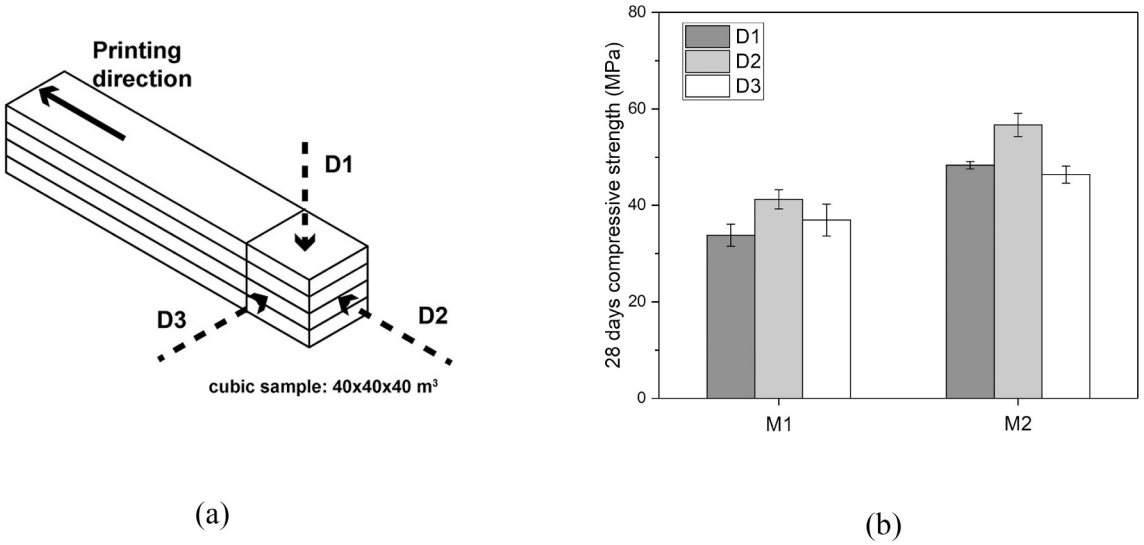

Fig. 21. (a) Illustration of three loading directions for compressive strength test; (b) 28 days compressive strength results of printed specimens. The specimens were sawn from the printed objects in Section 2.2 at the material age of 28 days (curing condition: 20 ± 2 °C, 99% relative humidity). All specimens had a dimension of 40×40×40 mm^3, and contained 3 interfaces and 4 layers. In each loading direction, the average value of compressive strength was calculated through 3 repeated tests. In total, 9 samples of each mixture were prepared and tested.

4. Conclusion

The goal of this paper is to systematically characterize and analyze the typical air void system of 3D printed cementitious materials, which have not been conducted previously. Two limestone and calcined clay-based 3D printable cementitious materials (M1 and M2) were used as examples in this context. Optical image scanning and X-ray computed tomography were employed to acquire digital images. Air void characteristics, i.e., content and distribution, pore size distribution, and shape properties, were quantified by different methods. According to the yielded results, the salient conclusions of this study can be drawn as follow:

- The results of local porosity and total air void content obtained by TS, CT-LP and CT-TP images illustrated a similar trend. Thus, material researchers could employ one of these approaches to quantify the air void content and distribution of 3D printed cementitious materials for selecting the optimal mix design and printing parameters.
- The air voids with the diameter in the range of 10 μm to1000 μm seemed to be evenly distributed in the layer, whereas the large air voids (1000–6000 μm) were formed mainly at the interface region (several large air voids were also found in the layer region), especially in sample M1. For both samples, the medium air voids (100–1000 μm) accounted for the highest air void content across measurements. Due to the possibility of merging and overlapping, the majority of air voids exhibited irregular and elongated shapes. This could be attributed to the extrusion and layer-wise manufacturing process in 3DCP.
- Both values of the average circularity and aspect ratio of small air voids (10–100 μm) were close to 1. This might be due to the small air voids made by only few pixels, which can not sufficiently indicate their intrinsic shape properties. In the case of medium and large air voids, the average circularity was decreased, and the average aspect ratio revealed an increasing trend with the increase of pore size.
- Thin section can be used for multi-scale analysis and observation of air voids, whereas the sample preparation is a challenge. The sample for X-ray computed tomography can be easily prepared.

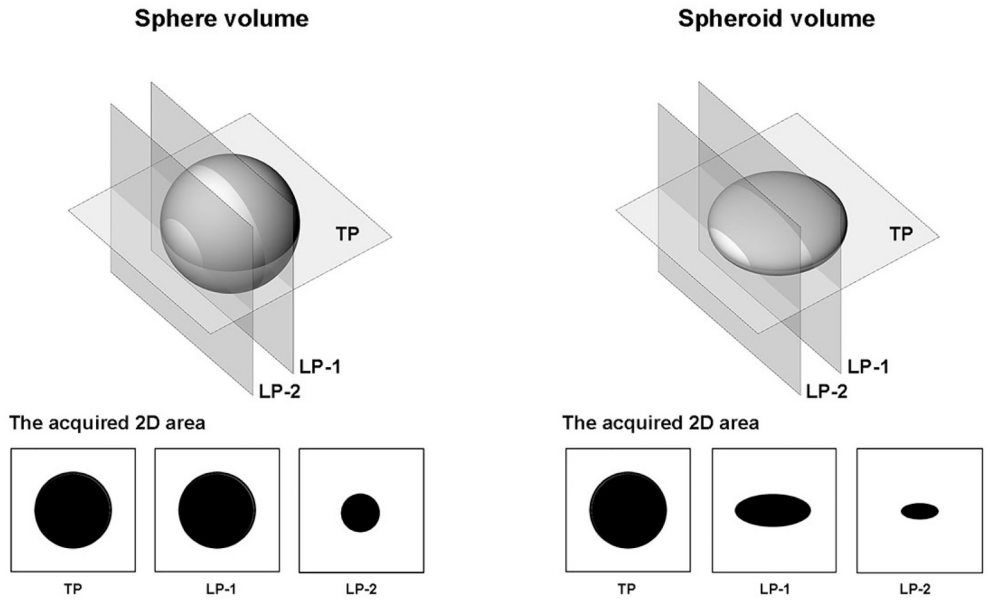

Fig. 22. Schematic description of the cross-sections of the sphere (left) and spheroid (right). For the spherical voids, only once the slice from the center plane of the sphere (TP and LP-1), the acquired 2D area (diameter) can represent the size of the corresponding air void. For the other anisotropic shapes, like spheroid, all acquired 2D areas can not indicate the real size of the air void.

Table 6
Comparative study of different approaches for characterizing air voids.

Image type	Optical image scanning - thin section	X-ray computed tomography	
	TS (LP)	CT-LP	CT-TP
Sample preparation			
Time (per sample)[a]	At least 36–48 h.	At most 0.5–1 h.	
Difficulty	Difficult, it requires experienced operators.	Simple, it requires less skilled labor.	
Image acquisition			
Time (per sample)[a]	Less than 0.5 h.	3.5–4 h (scanning+reconstruction).	
Difficulty	Simple, it requires a specialized operator.	Simple, it requires a certified operator.	
General evaluation			
Pros	(1) multi-scale observation and analysis. (2) possible to characterize the pores with small diameters (smaller than 10 μm is possible). (3) it is easy to segment sand grain and paste phases. (4) indicating the interlayer region directly.	(1) A sufficient number of slices. (2) Most of the air voids could be characterized (larger than several tens micron). (3) indicating the interlayer region directly.	(1) 3D analysis. (2) illustrating anisotropy of air voids. (3) Most of the air voids could be characterized (larger than several tens micron).
Cons	(1) 2D effects. (2) challenges with the sample preparation. (3) A limited number of slices.	(1) limited image resolution for big sample sizes. (2) 2D effects. (3) it is challenging to distinguish between sand and cement paste.	(1) limited image resolution for big sample sizes. (2) it is challenging to distinguish between sand and cement paste. (3) longer processing time.

[a] The required time for each sample mentioned in this table is based on the experiences of the authors in this paper, which could provide a reference for readers.

Nevertheless, the image resolution is limited for the sample with a relatively large size.

- In comparison with CT-TP images, the limitations of using TS and CT-LP images for air void analysis were highlighted. Due to the 2D effects, the measured results from TS and CT-LP images may lead to over−/under-estimation of local porosity and air void content. Additionally, the pore diameter obtained by TS and CT-LP images may not represent the real size of air voids. For pore morphology, the spatial anisotropy/heterogeneity of air voids may not be adequately indicated by TS and CT-LP images.

Data availability

The data that support the findings of this study are available from the corresponding author upon reasonable request.

Declaration of Competing Interest

None.

Acknowledgments

Yu Chen wants to acknowledge the funding supported by China Scholarship Council under grant No. 201807720005. Claudia Romero Rodriguez acknowledges the financial support from the Construction Technology Research Program funded by the Ministry of Land, Infrastructure, and Transport of the Korean Government under the grant 17SCIP-B103706-03. Burgess Pigment Company is thanked for the supply of the Optipozz®Burgess metakaolin.

References

[1] R.A. Buswell, W.R. Leal de Silva, S.Z. Jones, J. Dirrenberger, 3D printing using concrete extrusion: a roadmap for research, Cem. Concr. Res. 112 (2018) 37–49, https://doi.org/10.1016/j.cemconres.2018.05.006.

[2] G. De Schutter, K. Lesage, V. Mechtcherine, V.N. Nerella, G. Habert, I. Agusti-Juan, Vision of 3D printing with concrete — technical, economic and environmental potentials, Cem. Concr. Res. 112 (2018) 25–36, https://doi.org/10.1016/j.cemconres.2018.06.001.

[3] Y. Chen, F. Veer, O. Çopuroğlu, A critical review of 3D concrete printing as a low CO 2 concrete approach, Heron. 62 (2017) 167–194.

[4] Y. Chen, Z. Li, S. Chaves Figueiredo, O. Çopuroğlu, F. Veer, E. Schlangen, Limestone and calcined clay-based sustainable cementitious materials for 3D concrete printing: a fundamental study of Extrudability and early-age strength development, Appl. Sci. 9 (2019) 1809, https://doi.org/10.3390/app9091809.

[5] Y.W.D. Tay, Y. Qian, M.J. Tan, Printability region for 3D concrete printing using slump and slump flow test, Compos. Part B Eng. 174 (2019), https://doi.org/10.1016/j.compositesb.2019.106968.

[6] R.J.M. Wolfs, F.P. Bos, T.A.M. Salet, Hardened properties of 3D printed concrete: the influence of process parameters on interlayer adhesion, Cem. Concr. Res. 119 (2019) 132–140, https://doi.org/10.1016/j.cemconres.2019.02.017.

[7] B. Panda, J.H. Lim, M.J. Tan, Mechanical properties and deformation behaviour of early age concrete in the context of digital construction, Compos. Part B Eng. 165 (2019) 563–571, https://doi.org/10.1016/j.compositesb.2019.02.040.

[8] Z. Li, L. Wang, G. Ma, Mechanical improvement of continuous steel microcable reinforced geopolymer composites for 3D printing subjected to different loading conditions, Compos. Part B Eng. 187 (2020) 107796, https://doi.org/10.1016/j.compositesb.2020.107796.

[9] Y. Chen, S. Chaves Figueiredo, Z. Li, Z. Chang, K. Jansen, O. Çopuroğlu, E. Schlangen, Improving printability of limestone-calcined clay-based cementitious materials by using viscosity-modifying admixture, Cem. Concr. Res. 132 (2020) 106040, https://doi.org/10.1016/j.cemconres.2020.106040.

[10] A.V. Rahul, M. Santhanam, Evaluating the printability of concretes containing lightweight coarse aggregates, Cem. Concr. Compos. 109 (2020), 103570, https://doi.org/10.1016/j.cemconcomp.2020.103570.

[11] V.N. Nerella, V. Mechtcherine, Studying the Printability of Fresh Concrete for Formwork-Free Concrete Onsite 3D Printing Technology (CONPrint3D), in: 3D Concr. Print. Technol., Elsevier Inc., 2019, pp. 333–347, https://doi.org/10.1016/b978-0-12-815481-6.00016-6.

[12] P.C. Aïtcin, Entrained Air in Concrete: Rheology and Freezing Resistance, Elsevier Ltd, 2015, https://doi.org/10.1016/B978-0-08-100693-1.00006-0.

[13] Y. Chen, S. Chaves Figueiredo, Ç. Yalçinkaya, O. Çopuroğlu, F. Veer, E. Schlangen, The effect of viscosity-modifying admixture on the extrudability of limestone and calcined clay-based cementitious material for extrusion-based 3D concrete printing, Materials (Basel) 12 (2019) 1374, https://doi.org/10.3390/ma12091374.

[14] A. Perrot, D. Rangeard, V. Nerella, V. Mechtcherine, Extrusion of cement-based materials - an overview, RILEM Tech. Lett. 3 (2019) 91–97, https://doi.org/10.21809/rilemtechlett.2018.75.

[15] R. Kumar, B. Bhattacharjee, Porosity, pore size distribution and in situ strength of concrete, Cem. Concr. Res. 33 (2003) 155–164, https://doi.org/10.1016/S0008-8846(02)00942-0.

[16] E.K.K. Nambiar, K. Ramamurthy, Air-void characterisation of foam concrete, Cem. Concr. Res. 37 (2007) 221–230, https://doi.org/10.1016/j.cemconres.2006.10.009.

[17] K. Mehta, P.J.M. Monteiro, Concrete: Microstructure, Properties, and Materials, 3rd ed., McGraw-Hill, New York, 2006 https://doi.org/10.1036/0071462899.

[18] P. Choi, J.H. Yeon, K.K. Yun, Air-void structure, strength, and permeability of wet-mix shotcrete before and after shotcreting operation: the influences of silica fume and air-entraining agent, Cem. Concr. Compos. 70 (2016) 69–77, https://doi.org/10.1016/j.cemconcomp.2016.03.012.

[19] A. Perrot, D. Rangeard, A. Pierre, Structural built-up of cement-based materials used for 3D-printing extrusion techniques, Mater. Struct. 49 (2016) 1213–1220, https://doi.org/10.1617/s11527-015-0571-0.

[20] V.N. Nerella, S. Hempel, V. Mechtcherine, Effects of layer-interface properties on mechanical performance of concrete elements produced by extrusion-based 3D-printing, Constr. Build. Mater. 205 (2019) 586–601, https://doi.org/10.1016/j.conbuildmat.2019.01.235.

[21] N. Roussel, Rheological requirements for printable concretes, Cem. Concr. Res. 112 (2018) 76–85, https://doi.org/10.1016/j.cemconres.2018.04.005.

[22] Y.W.D. Tay, G.H.A. Ting, Y. Qian, B. Panda, L. He, M.J. Tan, Time gap effect on bond strength of 3D-printed concrete, Virt. Phys. Prototyp. 14 (2019) 104–113, https://doi.org/10.1080/17452759.2018.1500420.

[23] B. Panda, N.A.N. Mohamed, S.C. Paul, G.V.P.B. Singh, M.J. Tan, B. Šavija, The effect of material fresh properties and process parameters on buildability and interlayer adhesion of 3D printed concrete, Materials (Basel) 12 (2019) 2149, https://doi.org/10.3390/ma12132149.

[24] Y. Chen, K. Jansen, H. Zhang, C. Romero Rodriguez, Y. Gan, O. Çopuroğlu, E. Schlangen, Effect of printing parameters on interlayer bond strength of 3D printed limestone-calcined clay-based cementitious materials: an experimental and numerical study, Constr. Build. Mater. 262 (2020) 120094, https://doi.org/10.1016/j.conbuildmat.2020.120094.

[25] M.T. Ley, D. Welchel, J. Peery, J. LeFlore, Determining the air-void distribution in fresh concrete with the sequential air method, Constr. Build. Mater. 150 (2017) 723–737, https://doi.org/10.1016/j.conbuildmat.2017.06.037.

[26] N. Marinoni, A. Pavese, M. Foi, L. Trombino, Characterisation of mortar morphology in thin sections by digital image processing, Cem. Concr. Res. 35 (2005) 1613–1619, https://doi.org/10.1016/j.cemconres.2004.09.015.

[27] J.L. Chermant, L. Chermant, M. Coster, A.S. Dequiedt, C. Redon, Some fields of applications of automatic image analysis in civil engineering, Cem. Concr. Compos. 23 (2001) 157–169, https://doi.org/10.1016/S0958-9465(00)00059-7.

[28] M. Coster, J.L. Chermant, Image analysis and mathematical morphology for civil engineering materials, Cem. Concr. Compos. 23 (2001) 133–151, https://doi.org/10.1016/S0958-9465(00)00058-5.

[29] ASTM C457-98, Standard Test Method for Microscopical Determination of Parameters of the Air-Void System in Hardened Concrete, 1998, https://doi.org/10.1520/C0457-98.

[30] K.K. Aligizaki, P.D. Cady, Air content and size distribution of air voids in hardened cement pastes using the section-analysis method, Cem. Concr. Res. 29 (1999) 273–280, https://doi.org/10.1016/S0008-8846(98)00185-9.

[31] R. Pleau, M. Pigeon, J.L. Laurencot, Some findings on the usefulness of image analysis for determining the characteristics of the air-void system on hardened concrete, Cem. Concr. Compos. 23 (2001) 237–246, https://doi.org/10.1016/S0958-9465(00)00079-2.

[32] K. Peterson, J. Carlson, L. Sutter, T. Van Dam, Methods for threshold optimization for images collected from contrast enhanced concrete surfaces for air-void system characterization, Mater. Charact. 60 (2009) 710–715, https://doi.org/10.1016/j.matchar.2008.10.005.

[33] M. Wyrzykowski, R. Kiesewetter, B. Münch, R. Baumann, P. Lura, Pore structure of mortars with cellulose ether additions - study of the air-void structure, Cem. Concr. Compos. 62 (2015) 117–124, https://doi.org/10.1016/j.cemconcomp.2015.04.016.

[34] A. Koenig, Analysis of air voids in cementitious materials using micro X-ray computed tomography (μXCT), Constr. Build. Mater. 244 (2020) 118313, https://doi.org/10.1016/j.conbuildmat.2020.118313.

[35] S.Y. Chung, P. Sikora, T. Rucinska, D. Stephan, M. Abd Elrahman, Comparison of the pore size distributions of concretes with different air-entraining admixture dosages using 2D and 3D imaging approaches, Mater. Charact. 162 (2020) 110182, https://doi.org/10.1016/j.matchar.2020.110182.

[36] K.Y. Kim, T.S. Yun, J. Choo, D.H. Kang, H.S. Shin, Determination of air-void parameters of hardened cement-based materials using X-ray computed tomography, Constr. Build. Mater. 37 (2012) 93–101, https://doi.org/10.1016/j.conbuildmat.2012.07.012.

[37] T.S. Yun, K.Y. Kim, J. Choo, D.H. Kang, Quantifying the distribution of paste-void spacing of hardened cement paste using X-ray computed tomography, Mater. Charact. 73 (2012) 137–143, https://doi.org/10.1016/j.matchar.2012.08.008.

[38] G. Sokhansefat, M. Moradian, M. Finnell, A. Behravan, M.T. Ley, C. Lucero, J. Weiss, Using X-ray computed tomography to investigate mortar subjected to freeze-thaw cycles, Cem. Concr. Compos. 108 (2020) 103520, https://doi.org/10.1016/j.cemconcomp.2020.103520.

[39] A. du Plessis, W.P. Boshoff, A review of X-ray computed tomography of concrete and asphalt construction materials, Constr. Build. Mater. 199 (2019) 637–651, https://doi.org/10.1016/j.conbuildmat.2018.12.049.

[40] J. Van Der Putten, G. De Schutter, K. Van Tittelboom, Surface modification as a technique to improve inter-layer bonding strength in 3D printed cementitious materials, RILEM Tech. Lett. 4 (2019) 33–38, https://doi.org/10.21809/rilemtechlett.2019.84.

[41] H. Lee, J.-H.J. Kim, J.-H. Moon, W.-W. Kim, E.-A. Seo, Correlation between pore characteristics and tensile bond strength of additive manufactured mortar using X-ray computed tomography, Constr. Build. Mater. 226 (2019) 712–720, https://doi.org/10.1016/j.conbuildmat.2019.07.161.

[42] Y. Chen, C.R. Rodriguez, Z. Li, B. Chen, O. Çopuroğlu, E. Schlangen, Effect of different grade levels of calcined clays on fresh and hardened properties of ternary-blended cementitious materials for 3D printing, Cem. Concr. Compos. 114 (2020) 103708, https://doi.org/10.1016/j.cemconcomp.2020.103708.

[43] O. Çopuroğlu, Revealing the dark side of portlandite clusters in cement paste by circular polarization microscopy, Materials (Basel) 9 (2016), https://doi.org/10.3390/ma9030176.

[44] S. Chaves Figueiredo, O. Çopuroğlu, E. Schlangen, Effect of viscosity modifier admixture on Portland cement paste hydration and microstructure, Constr. Build. Mater. 212 (2019) 818–840, https://doi.org/10.1016/j.conbuildmat.2019.04.020.

[45] I. Arganda-Carreras, V. Kaynig, C. Rueden, K.W. Eliceiri, J. Schindelin, A. Cardona, H.S. Seung, Trainable Weka segmentation: a machine learning tool for microscopy pixel classification, Bioinformatics. 33 (2017) 2424–2426, https://doi.org/10.1093/bioinformatics/btx180.

[46] J. Van Der Putten, M. Deprez, V. Cnudde, G. De Schutter, K. Van Tittelboom, Microstructural characterization of 3D printed cementitious materials, Materials (Basel) 12 (2019) 2993, https://doi.org/10.3390/ma12182993.

[47] R. Gagné, Air Entraining Agents, Elsevier Ltd, 2015, https://doi.org/10.1016/B978-0-08-100693-1.00017-5.

[48] P.C. Nkinamubanzi, S. Mantellato, R.J. Flatt, Superplasticizers in practice, Elsevier Ltd, 2015, https://doi.org/10.1016/B978-0-08-100693-1.00016-3.

[49] M. Zhang, Y. He, G. Ye, D.A. Lange, K. Van Breugel, Computational investigation on mass diffusivity in Portland cement paste based on X-ray computed microtomography (μCT) image, Constr. Build. Mater. 27 (2012) 472–481, https://doi.org/10.1016/j.conbuildmat.2011.07.017.

[50] NEN-EN 480-11: 2005, Admixtures for Concrete, Mortar and Grout - Test Methods - Part 11: Determination of Air Void Characteristics in Hardened Concrete, 2005.